Marine Structures 80 (2021) 103083

Contents lists available at ScienceDirect

Marine Structures

journal homepage: www.elsevier.com/locate/marstruc

Validation of vessel seakeeping model tuning algorithm based on measurements at model scale

Xu Han [a,b,*], Bernt Johan Leira [a,b], Svein Sævik [a,b], Karl Erik Kaasen [b,c]

[a] Department of Marine Technology, Norwegian University of Science and Technology (NTNU), 7491 Trondheim, Norway
[b] Centre for Research-based Innovation on Marine Operations (SFI MOVE), Norway
[c] Department of Ships and Ocean Structures, SINTEF Ocean AS, Trondheim, Norway

ARTICLE INFO

Keywords:
Vessel seakeeping
Model tuning
Model-scale tests
Unscented transformation
Systematic errors

ABSTRACT

Wave-induced vessel motion prediction plays a critical role in ensuring safe marine operations. The operational limiting criteria can usually be calculated by applying presumed linearized vessel motion transfer functions based on the specified vessel loading condition, which may deviate from the real vessel condition when the operation is executed. Reducing the uncertainties of the onboard vessel loading condition can therefore improve the accuracy of vessel motion prediction and hence improve the safety and cost-efficiency for marine operations. However, parameters related to the onboard vessel loading condition can be difficult to measure directly, such as the center of gravity and moments of inertia. In addition, the hydrodynamic viscous damping terms are always subject to significant uncertainties and sometimes become critical for accurate vessel motion predictions. A very promising algorithm for the tuning of these important uncertain vessel parameters based on the unscented Kalman filter (UKF) that uses onboard vessel motion measurements and synchronous wave information was proposed and demonstrated previously by application to synthetic data. The present paper validates the UKF-based vessel seakeeping model tuning algorithm by considering measurements from model-scale seakeeping tests. Validation analyses demonstrate rational tuning results. The observed random errors and bias in relation to the measurement functions due to the applied simplification and linearization in the seakeeping simulations can lead to biased tuning. The importance of designing the state space and the measurement space is demonstrated by case studies. Due to the nonlinear relationship between the uncertain vessel parameters and the vessel motions, the tuning is shown to be sensitive to the mean state vector and selection of the surrounding sigma points.

1. Introduction

Improving the accuracy of vessel motion prediction is important for safe and cost-efficient marine operations. Compared with second-order difference-frequency motions, the wave-induced vessel responses in the wave frequency region are more difficult to control due to their high-frequency dynamics, which may therefore practically dominate the operational limiting criteria for typical marine operations such as transportation and lifting. Hence, the wave-induced vessel response at wave frequencies, i.e, the seakeeping performance, is focused on in the present paper. The uncertainty of this vessel motion prediction can be reduced by (1) reducing the uncertainties of the wave forecast; (2) improving the knowledge and control of the vessel conditions on board, such

* Corresponding author at: Department of Marine Technology, Norwegian University of Science and Technology (NTNU), 7491 Trondheim, Norway.
E-mail address: xu.han@ntnu.no (X. Han).

https://doi.org/10.1016/j.marstruc.2021.103083
Received 28 March 2021; Received in revised form 25 May 2021; Accepted 27 June 2021
Available online 20 August 2021

Nomenclature

α	Scaling factor for the UKF model
β	Hyperparameter in the UKF model in order to partially account for higher order statistical properties
$\beta_{44}^{'}$	The difference of the VERES estimated linearized additional roll damping coefficient from its true value
β_{dd}	The linearized additional damping coefficient at mode d
β_W	Wave direction w.r.t. vessel coordinate system
$\bar{\boldsymbol{P}}_k$	The state covariance matrix for $\bar{\boldsymbol{x}}_k$
$\bar{\boldsymbol{x}}_k$	The predicted system state for the kth update
$\boldsymbol{\mathcal{X}}_{k,i}$	The ith sigma point for the system state $\boldsymbol{x}_k$, i.e., the ith column of $\boldsymbol{\mathcal{X}}_k$
$\boldsymbol{\mathcal{X}}_k$	The sigma points for the system state $\boldsymbol{x}_k$
$\bar{\boldsymbol{\mathcal{Z}}}_k$	The predicted measurement vector estimated based on all sigma points $\boldsymbol{\mathcal{X}}_k$ for the kth update
$\boldsymbol{K}$	Kalman gain
$\boldsymbol{P}_k$	The system state covariance matrix for $\boldsymbol{x}_k$
$\boldsymbol{P}_{\boldsymbol{x}\boldsymbol{z}_k}$	The cross covariance matrix for the system state in state space and measurement space at kth measurement update step
$\boldsymbol{P}_{\boldsymbol{z}_k}$	The covariance matrix for the system state in measurement space at kth measurement update step
$\boldsymbol{Q}$	Process uncertainty covariance matrix
$\boldsymbol{R}$	Measurement uncertainty covariance matrix
$\boldsymbol{x}_k$	The system state after the kth update
$\boldsymbol{y}_k$	The residual at kth measurement update step
$\boldsymbol{Z}_{k,i}$	The predicted measurement vector at $\boldsymbol{\mathcal{X}}_{k,i}$
$\boldsymbol{Z}_{k,i}$	The predicted measurement vector based on the sigma point $\boldsymbol{\mathcal{X}}_{k,i}$
$\boldsymbol{z}_k$	The measurement vector containing the measured response characteristics at the kth update step
$\eta_d, \dot{\eta}_d, \ddot{\eta}_d$	Displacement, velocity, acceleration of response for mode d
κ	Hyperparameter in the UKF model
ω	Wave or response frequency
σ	The standard deviation of random variable
$\zeta(t)$	Wave elevation time series
$B_{a,dd}$	The linearized additional damping
$B_{cr,dd}$	The critical damping at mode d
d	The index of vessel rigid body modes. $d = 1$: surge, $d = 2$: sway, $d = 3$: heave, $d = 4$: roll, $d = 5$: pitch, $d = 6$: yaw
H_s	Significant wave height
$\boldsymbol{J}$	The total number of the considered measured response characteristics in the measurement space for one sea state
j	Index of the considered measured response characteristics
k	The index of each model test case
L_{PP}	Length between perpendiculars
N	The dimension of the system state
r_{44}	Radius of gyration for roll
r_{55}	Radius of gyration for pitch
$S_{\zeta\zeta}(\omega, \beta_W)$	Single-sided wave spectrum
$S_{XX}(\omega, \beta_W)$	Response spectrum for X
T_z	Zero-up-crossing period
T_p	Wave spectral peak period
w_i^c	The weight factor for state mean calculation at the ith sigma point, $i = 0, 1, 2, \ldots, 2N$
w_i^m	The weight factor for state covariance calculation at the ith sigma point, $i = 0, 1, 2, \ldots, 2N$
X	Vessel response
$x(t)$	Vessel response in form of time records, $x(t) \in \{\eta_d(t)\dot{\eta}_d, \ddot{\eta}_d\}$, $d \in \{3, 4, 5\}$ considered in the present paper
z_j	The considered jth quantity in the measurement space
BL	Baseline of vessel hull
CL	Centerline of vessel hull

COG	Center of gravity
DOF	Degree of freedom
FFT	Fast Fourier transform
OCV	Offshore Construction Vessel
ODSS	Onboard decision support system
PSD	Power spectral density
RAO	Response amplitude operator
UKF	Unscented Kalman filter
ZCG	Vertical coordinate of vessel COG

Many real-time onboard decision support systems (ODSSs) have been developed to assist marine operations based on vessel motion prediction. Computational efficiency is critical for a real-time vessel motion prediction, and therefore, the analytical model for vessel response prediction in an ODSS must be simplified. Normally, for marine operations, the wave-induced vessel response in the wave frequency region can be estimated based on linear transfer functions in relation to the wave elevation [1]. These linear transfer functions are also called response amplitude operators (RAOs), which can be calculated by seakeeping analysis software based on 3D panel methods or 2D strip theory [2–4].

Research on ODSSs [5–9] in recent decades has mainly focused on reducing the wave forecast uncertainty by, e.g., (1) developing high-fidelity wave forecast models [10] for forecasts of a few hours up to some days in advance; (2) calibrating the local alpha factor [1] with wave-measuring instruments deployed near the floater [11]; (3) measuring the wave field in front of the vessel and predicting the encountered waves through noncoherent or coherent radar systems or special cameras [8,12–14]; and (4) estimating the wave spectrum by applying the "ship as a wave buoy" analogy [15,16] and predicting the sea state by extrapolation. Similar to the design of marine operations, such an ODSS predicts wave-induced vessel responses based on the presumed deterministic vessel condition in terms of, e.g., the load distribution and linearized viscous damping, which may deviate from the real condition at the operation execution phase. These uncertainties of the vessel condition can significantly contribute to the errors of the predicted vessel motions and the consequent decision making [5,8,9]. Therefore, it is important to identify the on-site vessel conditions based on the information available on board and from the operation design phase. Some important vessel parameters such as the draft, trim, and heel can be measured directly, while other parameters such as the moment of inertia, center of gravity (COG), and linearized viscous damping may not be so easy to measure. Identification of these immeasurable vessel hydrodynamic parameters is therefore of great interest. For example, Xu and Soares [17] and Fossen et al. [18] proposed algorithms for the parameter identification of maneuvering and dynamic positioning scenarios; however, the responses in the wave frequency region were considered disturbances. Kaasen et al. [19] developed an automatic procedure for the tuning of a commercial simulation model based on output error minimization and tested it based on data from model tests, considering precise wave and vessel motion measurements, and accurate fundamental seakeeping theory.

Han et al. [20] proposed an algorithm for the identification of the immeasurable vessel seakeeping parameters based on onboard vessel motion measurements and wave information, considering data uncertainties. The uncertainties of the tuning results were quantified. The algorithm is based on discrete Bayesian inference with a predefined RAO database representing the parametric uncertainty ranges. Even though the parametric uncertainties can be quantified and the nonlinear relation between vessel parameters and responses can be captured, the algorithm faces a common challenge for large-dimensional problems due to discretization, i.e., the curse of dimensionality [21]. Therefore, Han et al. [22] developed a new and computationally efficient algorithm for the tuning and uncertainty quantification of the important vessel parameters based on the unscented transformation [23] and the unscented Kalman filter (UKF) [24] by assuming multivariate Gaussian distributed vessel variables. However, the algorithm has been demonstrated only in connection with case studies based on synthetic data. Method validations based on model-scale and full-scale measurements are therefore required.

This paper tests the performance of the UKF-based model tuning algorithm by applying measurements from model-scale seakeeping tests. The model tests are first described in Section 2. Then, the applied tuning algorithm is briefly summarized in Section 3. Afterwards, the scope of the validation analysis is described in Section 4. The results are shown and explained in Section 5. Finally, Section 6 summarizes the findings, discusses the limitations, and suggests future research work to modify the seakeeping model tuning algorithm.

2. Seakeeping model tests

Seakeeping model tests with zero forward speed for a state-of-the-art offshore construction vessel (OCV) were selected for the validation analyses of the UKF-based tuning algorithm. The vessel is approximately 150 m long and 27 m wide, and the tested loading condition approximately corresponds to a displacement of 20 000 m^3, a draft of 6.8 m, and a transverse metacentric height of 2.7 m. With one main work moonpool and two ROV moonpools, the OCV is also equipped with bilge keels (approximately 54 m long with a breadth of 1.0 m) and roll reduction tanks to reduce the roll motions.

Only one loading condition was considered in the model tests, with all three moonpools open. The model, at a scale of approximately 1:23, as illustrated in Fig. 1, was manufactured with 3 moonpools, 2 bow thruster tunnels, 3 stern thruster tunnels, 3

Fig. 1. Illustration of the seakeeping test.

Table 1
Seakeeping model tests performed for irregular waves.

k	Test No.	Spectral type	H_s [m]	T_p [s]	β_W [°]	Roll reduction tank
1	4000	JONSWAP	3	8	0	Frozen
2	4010	JONSWAP	3	10	0	Frozen
3	4020	JONSWAP	5	10	0	Frozen
4	4030	RECT	3	5–16	0	Frozen
5	4100	JONSWAP	3	8	15	Frozen
6	4110	JONSWAP	3	10	15	Frozen
7	4120	JONSWAP	5	10	15	Frozen
8	4130	RECT	3	5–16	15	Frozen
9	4200	JONSWAP	3	8	30	Frozen
10	4210	JONSWAP	3	10	30	Frozen
11	4220	RECT	3	5–16	30	Frozen
12	4300	JONSWAP	3	8	45	Frozen
13	4310	JONSWAP	3	10	45	Frozen
14	4320	RECT	3	5–16	45	Frozen
15	4401	JONSWAP	3	8	90	Frozen
16	4410	JONSWAP	3	10	90	Frozen
17	4420	RECT	3	5–16	90	Frozen
18	4500	JONSWAP	3	8	150	Frozen
19	4510	JONSWAP	3	10	150	Frozen
20	4600	JONSWAP	3	8	165	Frozen
21	4610	JONSWAP	3	10	165	Frozen
22	4700	JONSWAP	3	8	180	Frozen
23	4710	JONSWAP	3	10	180	Frozen
24	4720	RECT	3	5–16	180	Frozen

roll reduction tanks, and bilge keels. Only cases with the roll reduction tanks deactivated (namely, "frozen") were considered in the validation analyses. The model was weighed and balanced to obtain the specified loading condition as accurately as possible, w.r.t. the COG, radii of gyration for the roll and pitch, and volume displacement. The model tests were performed with only long-crested waves and without disturbance from current or wind. The main focus of the tests was to investigate the local effect of moonpool resonance. Therefore, most tests were carried out for sea states with peak periods (T_p) around the moonpool resonance periods, i.e., between 8 s and 10 s. Narrowband JONSWAP wave spectra with a peak enhancement factor of 3.3 were applied for the tests. For each wave direction β_W, an additional test case was conducted with a broadband and approximately rectangular wave spectrum (denoted by "RECT") for wave periods from 5 s to 16 s with a significant wave height (H_s) of 3 m. The considered test cases are summarized in Table 1.

A reference coordinate system was defined for the convenience of reporting. All the quantities reported hereafter correspond to this coordinate system. The origin of the coordinate system is at the baseline (BL) of the midship ($L_{pp}/2$) along the longitudinal symmetric axis, i.e., the centerline (CL). The positive x-axis points towards the bow, positive y-axis points towards port, and positive z-axis points upwards vertically. The definition of β_W in the present paper follows the coming-from convention, i.e., 0° for head sea, 180° for following sea, and 90° for beam seas coming from the port side.

A soft mooring system consisting of 4 horizontal springs was used to keep the model on station. This mooring system leads to low-frequency motions in surge, sway and yaw at periods of approximately 100 s. In the model tests, vessel motions and wave elevations were recorded in the form of time series. The measurement instruments, locations (at full scale) and quantities are summarized in Table 2.

Measurements from accelerometers were used for quality control of the OQUS camera outputs. The wave elevation measurements from the wave probes were calibrated prior to the model tests, e.g., as illustrated in Fig. 2. The OQUS camera measured motion signals of heave [m], roll [deg], and pitch [deg], and the calibrated wave elevation [m] measurements were used in the validation analyses. The nominal accuracy of the OQUS camera measurements was 0.8 mm for translational motions and 0.1° for angular

Table 2
Summary of measurements.

Instrument	Location [m]	Quantities
OQUS camera[a]	(0, 0, 0)	(Angular) Displacements of 6 DOFs[b]
Accelerometers	(−58.6, −10.4, 7.5)	Translational accelerations
Probes	8 port side, 2 starboard side, 1 in each of the moonpools	Relative water elevations

[a]OQUS electronic-optical positioning system.
[b]DOF: degree of freedom.

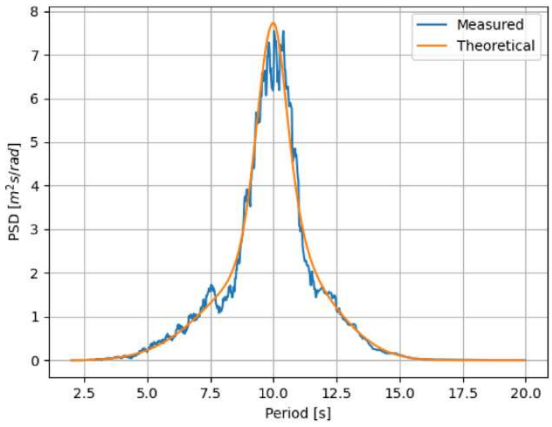

Fig. 2. Comparison of wave spectra between the theoretical and the measured for Test 4020. PSD: power spectral density. (For interpretation of the references to color in this figure legend, the reader is referred to the web version of this article.)

motions, while the accuracy of the wave measurements was 1 mm. All the measurements were transferred to full scale according to the Froude scaling laws [25]. At full scale, the duration of each seakeeping test was approximately 4500 s and the associated sampling frequency was approximately 41.6 Hz. The numerical seakeeping models were also made at full scale.

3. Formulation of the tuning algorithm

Han et al. [22] proposed a tuning algorithm based on the unscented transformation [23] and the corresponding scaled unscented Kalman filter (UKF) [24], which is computationally efficient for large-dimensional problems and guarantees second-order approximation accuracy for nonlinear systems. The UKF, belonging to the family of sigma-point Kalman filters [26], linearizes a model by implicitly applying weighted statistical linear regression based on the information at several deterministic points (i.e., the so-called sigma points). It uses nonlinear functions explicitly at the sigma points and therefore does not require the linear algebra formulation. This has been shown as an advantage for the problem of seakeeping model tuning heavily involving complex and state-dependent measurement functions [22].

The original tuning procedure contains a weather update step so that the wave characteristics for a sea state (e.g., H_s, T_p, and β_W) are included in the system state and tuned together with the uncertain vessel parameters [22]. As shown in Fig. 2, the wave measurements are subjected to insignificant uncertainties under laboratory conditions. Therefore, wave characteristics are not included in the system state, and the weather update step becomes irrelevant. Instead, the measured wave time series $\zeta(t)$ is considered as an input affecting the measurement function, which is used as part of the measurement update step. The complete tuning procedure for one sea state indexed by $k+1$ is illustrated in Fig. 3. The tuning process mainly consists of 3 steps, i.e., calculation of the sigma points and their weight factors, system propagation, and measurement update.

The state vector includes uncertain vessel parameters such as those related to the inertia distribution and the linearized viscous damping terms. The initial state vector and the state covariance matrix are denoted by $\boldsymbol{x}_0$ and $\boldsymbol{P}_0$, respectively. The state vector and covariance matrix after updating by k sea states are denoted by $\boldsymbol{x}_k$ and $\boldsymbol{P}_k$, respectively. Each sea state is assumed stationary and independent from other sea states.

When measurements of vessel responses and wave elevations are acquired for sea state $k+1$, the sigma points should be calculated based on the updated N-dimensional state $\boldsymbol{x}_k$ and $\boldsymbol{P}_k$:

$$\mathcal{X}_{k+1,0} = \boldsymbol{x}_k \tag{1a}$$

$$\mathcal{X}_{k+1,i} = \begin{cases} \boldsymbol{x}_k + \left[\sqrt{(N+\lambda)\boldsymbol{P}_k}\right]_i & \text{for } i = 1, 2, \ldots, N \\ \boldsymbol{x}_k - \left[\sqrt{(N+\lambda)\boldsymbol{P}_k}\right]_{i-N} & \text{for } i = N+1, \ldots, 2N \end{cases} \tag{1b}$$

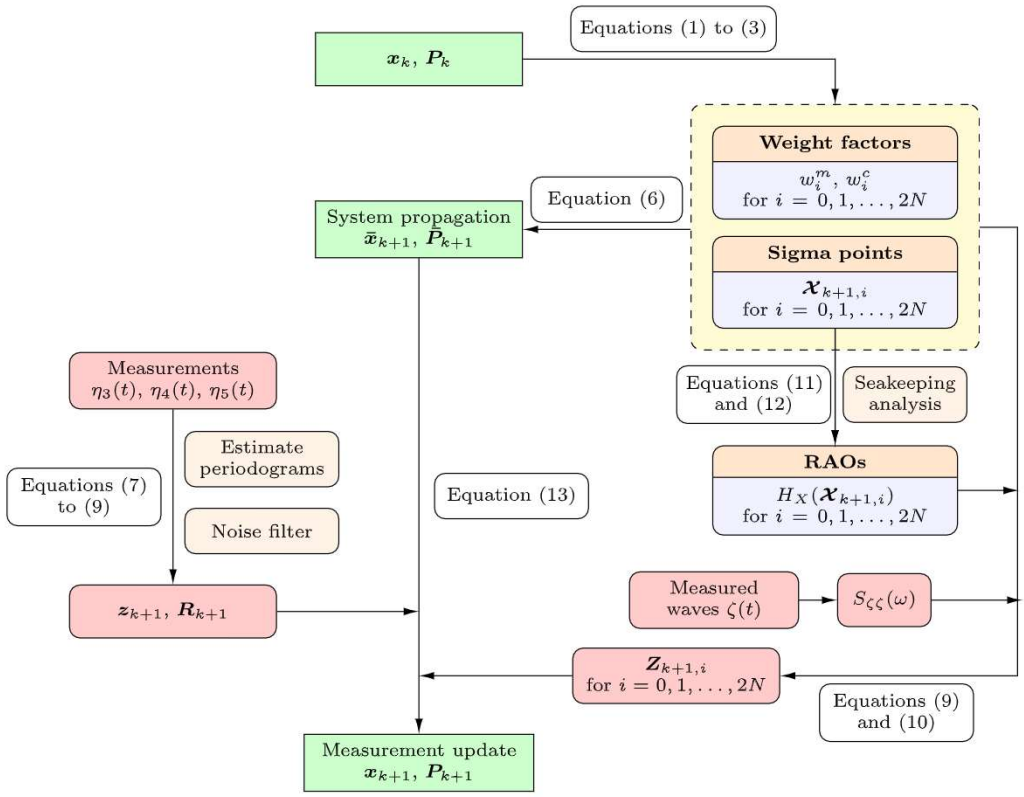

Fig. 3. The process of tuning vessel seakeeping model parameters, together with the quantification of uncertainties.

$$\mathcal{X}_{k+1} = [\mathcal{X}_{k+1,0} \quad \mathcal{X}_{k+1,1} \quad \cdots \quad \mathcal{X}_{k+1,2N}] \tag{1c}$$

where $\left[\sqrt{(N+\lambda)\boldsymbol{P}_k}\right]_i$ is the ith column (or row) of the matrix square root of $(N+\lambda)\boldsymbol{P}_k$. Each sigma point $\mathcal{X}_{k+1,i}$ for $i \in \{0, 1, \ldots, 2N\}$ is deterministically selected according to Eq. (1a) or Eq. (1b). The matrix $\mathcal{X}_{k+1}$ has a size of $N \times (2N+1)$, where each column represents a sigma point. The hyperparameter λ in Eq. (1) is calculated by:

$$\lambda = \alpha^2(N + \kappa) - N \tag{2}$$

where α is the scaling factor, the hyperparameter κ is normally set to either $3 - N$ or 0, and $\kappa \neq -N$. The corresponding weight factors for the sigma points to be used for estimation of the mean and the covariance can be calculated by:

$$w_0^m = \frac{\lambda}{\lambda + N} \tag{3a}$$

$$w_0^c = \frac{\lambda}{\lambda + N} + 1 - \alpha^2 + \beta \tag{3b}$$

$$w_i^c = w_i^m = \frac{1}{2(\lambda + N)} \tag{3c}$$

where w^m denotes the weight factors for the mean calculation, w^c denotes the weight factors for the covariance matrix calculation, and $i = 1, 2, \ldots, 2N$. The hyperparameter β equals to 2 for Gaussian distributed variables [24]. The weight factors depend only on the dimension and the values of the UKF-related hyperparameters.

With the deterministically selected sigma points and their corresponding weight factors, the system state can be predicted for sea state number $k + 1$ through the system propagation step by:

$$\bar{\boldsymbol{x}}_{k+1} = \sum_{i=0}^{2N} w_i^m f(\mathcal{X}_{k+1,i}) \tag{4a}$$

$$\bar{\boldsymbol{P}}_{k+1} = \sum_{i=0}^{2N} w_i^c (f(\mathcal{X}_{k+1,i}) - \bar{\boldsymbol{x}}_{k+1})(f(\mathcal{X}_{k+1,i}) - \bar{\boldsymbol{x}}_{k+1})^\top + \boldsymbol{Q} \tag{4b}$$

where $\bar{\boldsymbol{x}}_{k+1}$ and $\bar{\boldsymbol{P}}_{k+1}$ are the predicted state vector and covariance matrix. $f()$ is the process model, i.e., the state propagation function. $\boldsymbol{Q}$ is the process uncertainty covariance matrix representing the process disturbance and the process model uncertainties.

Eq. (4) is generally valid for any nonlinear process models. However, the system propagation step can be very much simplified when the propagation function is linear, such as the presently considered tuning of the vessel seakeeping model parameters. Stationary sea states and vessel conditions are assumed, leading to a simple linear function:

$$f(\boldsymbol{\mathcal{X}}_{k+1,i}) = \boldsymbol{I}_N \boldsymbol{\mathcal{X}}_{k+1,i} = \boldsymbol{\mathcal{X}}_{k+1,i} \tag{5}$$

where $\boldsymbol{I}_N$ is an N-dimensional identity matrix. Consequently, Eq. (4) can be replaced by Eq. (6) for the present study:

$$\bar{\boldsymbol{x}}_{k+1} = \boldsymbol{x}_k \tag{6a}$$

$$\bar{\boldsymbol{P}}_{k+1} = \boldsymbol{P}_k + \boldsymbol{Q} \tag{6b}$$

Following the system propagation, the system state can now be updated through the measurement update step by application of the acquired wave and vessel motion measurements for sea state $k+1$. As illustrated in Fig. 3, heave $\eta_3(t)$, roll $\eta_4(t)$, and pitch $\eta_5(t)$ measured by the OQUS camera and wave elevations $\zeta(t)$ measured by the probes are used in the validation analyses. Second-order surge, sway, and yaw motions are significant. Therefore, the corresponding measurements are excluded. Considering that the measurements are associated with high accuracy due to the application of advanced instruments, calibration, and quality control under laboratory conditions as mentioned in Section 2, signal noise is considered negligible. A previous vessel seakeeping parametric sensitivity study [27] suggests including the derivative information regarding the vessel motions (e.g., the velocity and acceleration) to improve the tuning accuracy for the uncertain parameters. Therefore, in the validation analyses, the measurement space in the UKF-based tuning model is considered to include the standard deviations of the (angular) displacement, velocity, acceleration, and corresponding zero-up-crossing periods (T_z) for heave, roll, and pitch in the wave frequency range. The measurement space and the measurement vector $\boldsymbol{z}$ can be formulated as:

$$\begin{aligned} \boldsymbol{z} &= [z_1 \quad z_2 \quad \dots \quad z_j \quad \dots \quad z_J]^\top \\ z_j &\in \{\sigma_{\eta_3}, \sigma_{\dot{\eta}_3}, \sigma_{\ddot{\eta}_3}, \sigma_{\eta_4}, \sigma_{\dot{\eta}_4}, \sigma_{\ddot{\eta}_4}, \dots, T_{z(\eta_3)}, T_{z(\eta_4)}, \dots\} \end{aligned} \tag{7}$$

where σ is the standard deviation and η_d, $\dot{\eta}_d$, $\ddot{\eta}_d$ represent the (angular) displacement, velocity, and acceleration for the considered responses in 6 DOFs. d is usually referred to as the index of the vessel rigid body modes. $d = 1, 2, 3, 4, 5, 6$ correspond to surge, sway, heave, roll, pitch, and yaw, respectively. The vessel motions of mode d are also referred to as the motions in the dth DOF. $j = 1, 2, \dots, J$, where J is the number of considered measured response characteristics in the measurement space for one sea state. Selecting the quantities for the measurement vector can be critical to the tuning results, especially when the measurement function is subject to significant uncertainty, e.g., due to simplification of the seakeeping model.

In the following, a scalar quantity X denotes a vessel response, with $X \in \{\eta_d, \dot{\eta}_d, \ddot{\eta}_d\}$ and $d = \{1, 2, \dots, 6\}$. $X(\omega)$ represents the response in the frequency domain, while $x(t)$ represents the corresponding time domain signal. The numerical differentiation of discrete signals $x(t)$ is well known to generate very high noises. These noises are usually at high frequencies and can be distinguished outside the frequency interval of the real motions. Therefore, the measured $\eta_3(t)$, $\eta_4(t)$, $\eta_5(t)$, and $\zeta(t)$ are first transferred to the frequency domain by estimating their periodograms [28]. The corresponding power spectral densities (PSDs), i.e., $S_{\eta_3\eta_3}(\omega)$, $S_{\eta_4\eta_4}(\omega)$, $S_{\eta_5\eta_5}(\omega)$, and $S_{\zeta\zeta}(\omega)$, are subsequently calculated. Then, the corresponding spectra of the velocities and accelerations can be calculated by:

$$S_{\dot{X}\dot{X}}(\omega) = \omega^2 S_{XX}(\omega) \tag{8a}$$

$$S_{\ddot{X}\ddot{X}}(\omega) = \omega^4 S_{XX}(\omega) \tag{8b}$$

where $\dot{X}(\omega)$ in the frequency domain represents the first derivative of X, i.e., $\dot{x}(t) = \frac{d\,x(t)}{d\,t}$ in the time domain, while $\ddot{X}(\omega)$ represents its second derivative, i.e., $\ddot{x}(t) = \frac{d^2\,x(t)}{d\,t^2}$. The PSDs outside the wave frequencies should be removed before the measurement update step. This is considered equivalent to a fast Fourier transform (FFT) bandpass filter. Then, the quantities in the measurement space $\boldsymbol{z}$ can be calculated:

$$\sigma_X = \sqrt{m_0} \tag{9a}$$

$$T_{z(X)} = 2\pi\sqrt{\frac{m_0}{m_2}} \tag{9b}$$

$$m_0 = \sum_{\omega} S_{XX}(\omega)\Delta\omega \tag{9c}$$

$$m_2 = \sum_{\omega} \omega^2 S_{XX}(\omega)\Delta\omega \tag{9d}$$

Once the quantities of the measurement space have been selected, the system state including the uncertain vessel parameters should be transferred from the state space to the measurement space by applying the measurement functions. It is obvious that these measurement functions are highly nonlinear and dependent on the state as well. The system state in the measurement space is called "the predicted measurements", denoted by $\boldsymbol{\mathcal{Z}}$. First, the response spectrum should be calculated for each sigma point $\boldsymbol{\mathcal{X}}_{k+1,i}$:

$$S_{XX,i}(\omega) = |H_X(\omega, \beta_W | \boldsymbol{\mathcal{X}}_{k+1,i})|^2 S_{\zeta\zeta,k+1}(\omega, \beta_W) \tag{10}$$

where $S_{\zeta\zeta,k+1}(\omega, \beta_W)$ is the wave spectrum for sea state $k+1$, which is calculated based on the periodogram of the calibrated probe measurements. The linear transfer function $H_X(\omega, \beta_W | \boldsymbol{\mathcal{X}}_{k+1,i})$ for the response X varies with the sigma point $\boldsymbol{\mathcal{X}}_{k+1,i}$. Subsequently, the

elements of the predicted measurements can be calculated based on Eq. (9). At each sigma point $\mathcal{X}_{k+1,i}$, the predicted measurement vector can be assembled according to Eq. (7) based on the selected measurement space, denoted by $\mathcal{Z}_{k+1,i}$.

As illustrated in Fig. 3, seakeeping analysis is carried out at each sigma point $\mathcal{X}_{k+1,i}$ to obtain $|H_X(\omega, \beta_W|\mathcal{X}_{k+1,i})|$. The simulated linear transfer functions of heave $H_{\eta_3^*}(\omega)$ are reported at a dedicated location on the vessel, depending on the software and the numerical modeling. The superscript $*$ for η_3^* indicates that the software-reported heave RAO may be at a location different from the measured location. Therefore, the software-calculated complex-valued heave RAOs must be transferred to the measured location, i.e., the origin of the reference coordinate system in the present case studies, by:

$$H_{\eta_3}(\omega) = H_{\eta_3^*}(\omega) - y_0 H_{\eta_4}(\omega) + x_0 H_{\eta_5}(\omega) \tag{11}$$

where $H_{\eta_3}(\omega)$ is the complex-valued heave motion RAO at the OQUS-measured location, i.e., (0, 0, 0) in the reference coordinate system. (x_0, y_0, z_0) are the coordinates of the software-reported RAOs in the same reference coordinate system. The roll and pitch RAOs remain the same at different locations on a rigid body. Afterwards, the RAO amplitudes of the velocity and acceleration can be calculated based on the (angular) displacement:

$$|H_{\dot{X}}(\omega)| = \omega |H_X(\omega)| \tag{12a}$$

$$|H_{\ddot{X}}(\omega)| = \omega^2 |H_X(\omega)| \tag{12b}$$

Eqs. (7) and (9) to (12) should be treated as a complete set of the measurement functions to calculate the predicted measurement vector $\mathcal{Z}_{k+1,i}$ at each sigma point, while Eqs. (7) to (9) provide the procedure to calculate the measurement vector z_{k+1}. The measurement functions are very difficult to express in a compact mathematical formulation because (1) many different response characteristics can be included in the measurement space (e.g., σ and T_z); (2) it involves seakeeping simulations, rigid body motion transformations, derivative calculations, etc.; and (3) the applied RAOs again depend on the state and subsequent selection of the sigma points. Finally, the measurement update step can be performed based on:

$$\bar{\mathcal{Z}}_{k+1} = \sum_{i=0}^{2N} w_i^m \mathcal{Z}_{k+1,i} \tag{13a}$$

$$\boldsymbol{y}_{k+1} = \boldsymbol{z}_{k+1} - \bar{\mathcal{Z}}_{k+1} \tag{13b}$$

$$\boldsymbol{P}_{\boldsymbol{z}_{k+1}} = \sum_{i=0}^{2N} w_i^c (\mathcal{Z}_{k+1,i} - \bar{\mathcal{Z}}_{k+1})(\mathcal{Z}_{k+1,i} - \bar{\mathcal{Z}}_{k+1})^\top + \boldsymbol{R}_{k+1} \tag{13c}$$

$$\boldsymbol{P}_{\boldsymbol{x}\boldsymbol{z}_{k+1}} = \sum_{i=0}^{2N} w_i^c (\mathcal{X}_{k+1,i} - \bar{\boldsymbol{x}}_{k+1})(\mathcal{Z}_{k+1,i} - \bar{\mathcal{Z}}_{k+1})^\top \tag{13d}$$

$$\boldsymbol{K} = \boldsymbol{P}_{\boldsymbol{x}\boldsymbol{z}_{k+1}} \boldsymbol{P}_{\boldsymbol{z}_{k+1}}^{-1} \tag{13e}$$

$$\boldsymbol{x}_{k+1} = \bar{\boldsymbol{x}}_{k+1} + \boldsymbol{K}\boldsymbol{y}_{k+1} \tag{13f}$$

$$\boldsymbol{P}_{k+1} = \bar{\boldsymbol{P}}_{k+1} - \boldsymbol{K}\boldsymbol{P}_{\boldsymbol{z}_{k+1}}\boldsymbol{K}^\top \tag{13g}$$

where the residual $\boldsymbol{y}_{k+1}$ is the difference between the predicted measurement $\bar{\mathcal{Z}}_{k+1}$ and the realized measurement vector $\boldsymbol{z}_{k+1}$ in the measurement space and $\boldsymbol{R}_{k+1}$ represents the uncertainties from the measurements and the measurement functions. $\boldsymbol{P}_{\boldsymbol{z}_{k+1}} \in \mathbb{R}^{J\times J}$ is the covariance matrix of the sigma points in the measurement space, and $\boldsymbol{P}_{\boldsymbol{x}\boldsymbol{z}_{k+1}} \in \mathbb{R}^{N\times J}$ is the cross covariance of the state and the measurement. $\boldsymbol{x}_{k+1}$ and $\boldsymbol{P}_{k+1}$ are the updated state mean and covariance matrix based on the calculated Kalman gain $\boldsymbol{K}$ for the sea state indexed by $k+1$.

4. Scope of the validation analysis

The vessel seakeeping model tuning algorithm described in Section 3 was validated based on the seakeeping (zero speed) model tests described in Section 2.

4.1. Numerical seakeeping model and response measurements

In the validation analyses, the RAOs at the sigma points were calculated by means of the ShipX (VERES) software developed by SINTEF Ocean [3] and based on 2D strip theory. The adequate meshing of the ShipX model is illustrated in Fig. 4.

A simplified representation of the moonpools was applied in ShipX. The locations and dimensions of the three moonpools were specified as inputs to ShipX in order to approximately obtain the correct vessel displacement volume and longitudinal center of buoyancy [29]. Due to the relatively small volume ratio between the moonpools and vessel, the coupling effects between the moonpool and vessel responses were considered small [30]. Ravinthrakumar et al. [31] also shows negligible coupling effects between vessel motions and moonpool response for a volume ratio less than 4.5%. However, the coupling effects are not only dependent on the volume ratio but also highly dependent on the location of the moonpool(s) and the wave heading [32]. Such coupling effects mostly influence the vessel motions (e.g., heave and pitch) around the moonpool resonance periods with respect to the piston and sloshing modes. It is believed that the coupling between moonpool and roll can be much more complicated

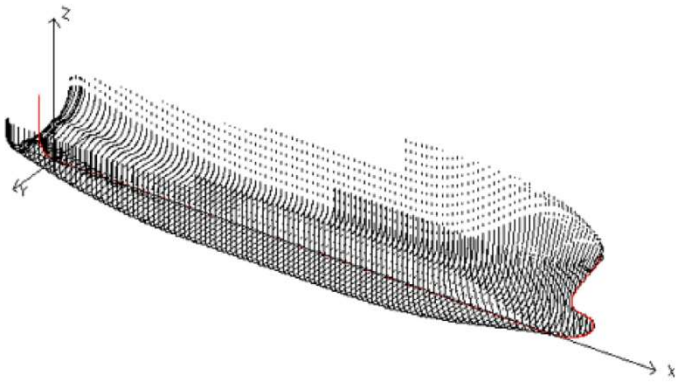

Fig. 4. Screenshot of the ShipX strip model.

owing to (1) the significant nonlinear sloshing effects from the water in the moonpool on the roll motion; (2) the significant viscous damping contributed by the sharp edges of the moonpools; and (3) the nonlinear swirling effects. Moreover, for vessels with multiple moonpools, even though the moonpool arrangement is normally symmetric with respect to the centerline, the moonpool response can be different between symmetric moonpools for oblique and beam seas due to the shielding effects and the encountered wave phase differences. All of these facts make the roll motion estimation complicated. Therefore, this simplified ShipX model is expected to have relatively high uncertainties associated with the roll RAO estimation.

VERES in ShipX is based on linear potential theory with the assumption of inviscid and incompressible fluid and irrotational flow condition [33]. However, damping terms in addition to that based on linear potential theory may play critical roles in the vessel motion estimation, particularly for the roll around its resonance [34]. This "additional" damping is in fact nonlinear due to viscous effects, dependent on the amplitudes and frequencies of the considered vessel motion velocities and waves. The stochastic linearization technique [35] is usually applied to express the relationship between vessel motion and wave elevation in the frequency domain. Consequently, this linearized "additional" damping becomes sea-state dependent. Han et al. [36] proposed to a method to handle such important sea-state dependent parameters in the tuning process based on discrete Bayesian inference so that the prediction accuracy for those parameters can be improved and quantified by the tuning results at the observed sea states. The linearized additional damping coefficient β_{dd} for mode d is defined as the ratio between the linearized additional damping and the critical damping for mode d as a percentage (i.e., 100 times the ratio):

$$\beta_{dd} = \frac{B_{a,dd}}{B_{cr,dd}} \times 100\ [\%] \tag{14a}$$

$$B_{cr,dd} = 2\sqrt{(M_{dd} + A_{dd}(\infty))C_{dd}} \tag{14b}$$

where M_{dd}, A_{dd}, and C_{dd} are the vessel inertia, added mass, and restoring stiffness for the motion mode d, respectively. The vessel added mass is frequency dependent. For simplicity, a constant added mass A_{dd} for each motion mode d has been considered in Eq. (14b), taken as the added mass at the infinite frequency $\omega \to \infty$. $B_{a,dd}$ is the linearized additional damping, and $B_{cr,dd}$ is the critical damping for the dth DOF. In the case studies, constant values of $B_{cr,dd}$ for $d = 3,4,5$ were applied independent of tuning results. In fact, it is mostly important to find the best $B_{a,dd}$ to represent the vessel dynamics for the present vessel and wave conditions. β_{dd} was introduced mainly to ensure that all the parameters considered in the system state space are of similar magnitudes for the purpose of numerical stability, as explained in Section 4.2. Tuning of β_{dd} with reference to a constant $B_{cr,dd}$ helps revealing the change of $B_{a,dd}$ through tuning simulations.

The geometry and location of the bilge keels are specified in the ShipX model. VERES estimates the linearized viscous roll damping from the hull and bilge keels based on Ikeda's formulas [37–40]. Hence, β_{44} is automatically included in the simulation based on the semiempirical solutions. However, this estimation of β_{44} is still subject to considerable uncertainties. Instead, for the validation analysis in the application of the VERES simulations, the parameter β'_{44} is considered in the state vector, representing the error of the additional roll damping coefficient between the VERES estimated and the true value:

$$\beta'_{44} = \beta_{44} - \beta^{VER}_{44} \tag{15}$$

where β_{44} is the previously defined additional roll damping and β^{VER}_{44} is the additional roll damping estimated by ShipX (VERES). β'_{44} may therefore be expected to vary around zero.

For verification of the model, the resonance periods of the output roll ($\beta_W = 90°$) and pitch ($\beta_W = 0°$) RAOs were first benchmarked based on the roll and pitch decay tests. RAOs are always reported at the COG in VERES, i.e., (−3.81 m, 0, 10.82 m) with respect to the reference coordinate system defined in Section 2. The heave RAOs should therefore be transferred to the reference coordinate system origin according to Eq. (11). The set of VERES-simulated RAOs based on the tested loading condition and benchmarked based on the decay tests are hereby referred to as the "reference" RAOs.

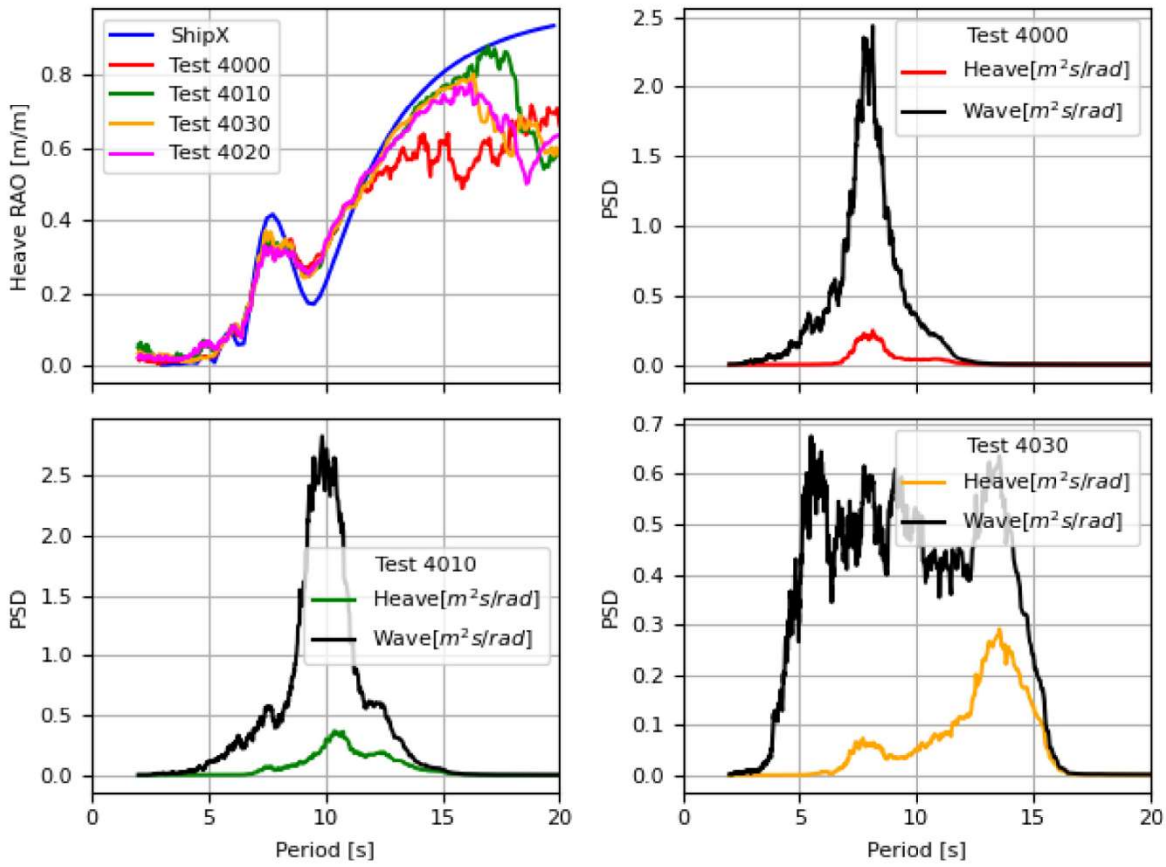

Fig. 5. The measured heave RAOs and the reference heave RAO from the ShipX (VERES) simulation at head sea (top left), and the power spectral densities (PSDs) of the measured waves and heave motions for Tests 4000, 4010, and 4030. (For interpretation of the references to color in this figure legend, the reader is referred to the web version of this article.)

The applied unidirectional wave conditions in the laboratory provide the perfect opportunity to compare the measured RAOs with the corresponding simulated RAOs from the seakeeping software. The measured RAO amplitudes can therefore be calculated by:

$$|H_X(\omega)| = \sqrt{\frac{S_{XX}(\omega)}{S_{\zeta\zeta}(\omega)}} \tag{16}$$

where $S_{XX}(\omega)$ and $S_{\zeta\zeta}(\omega)$ are power spectral densities of the response X and wave elevation ζ from the measurements. Several critical issues are hence identified: (1) numerical error magnification due to very small wave energies away from the peak frequencies; (2) second-order effect on the roll motion; (3) moonpool coupling effects on the vessel motions; and (4) generally larger estimation errors on the roll motion. Detailed explanations are given in the following.

The reference RAOs for heave and pitch are shown under the head sea condition in Figs. 5 and 6, while the reference roll RAO is shown for beam sea in Fig. 7, with comparison of the RAOs calculated for the relevant test cases. Due to the limited dimensions of the ocean basin laboratory and the applied model scale, wave components with wave periods larger than 15 s at full scale become unreliable. Therefore, the vessel response and wave components with periods larger than 15 s were disregarded in the tuning process. When the wave PSD is sufficiently small, numerical issues may occur if applying Eq. (16). For example, as illustrated in Fig. 6, the measured pitch RAO amplitudes at small periods (i.e., 2 to 5 s) from Test 4020 are overestimated due to the very small wave energies and measurement errors. Large RAO estimation errors can also be observed at large periods (e.g., > 15 s) due to the same numerical issue. However, it is worth mentioning that the proposed tuning algorithm may not be highly influenced by these numerical errors because the measurement space focuses on the overall characteristics of the response spectra (e.g., parameters related to m_0 and m_2) instead of directly calculating the RAOs based on Eq. (16). Hence, the small energies or measurement errors usually do not significantly influence those characteristics.

However, special attention should be paid to the measured roll motions, as shown in Fig. 7. Very large roll motions are observed around the resonance, i.e., at approximately 15 s, where very little wave energies exist. These significant roll motions outside the main wave frequency range are believed to be due to the second-order difference-frequency responses from the interactions of wave

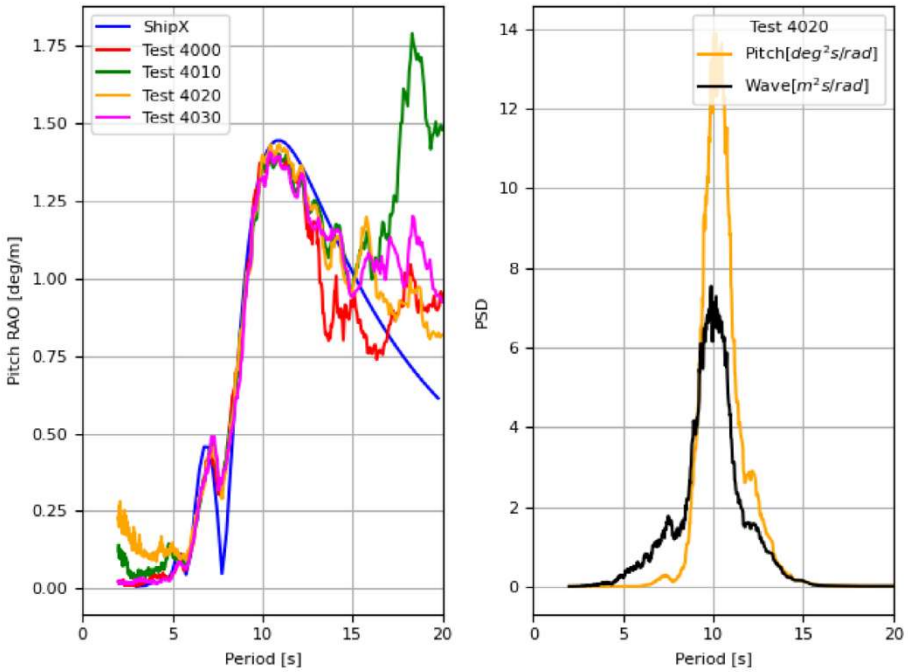

Fig. 6. The measured pitch RAOs and the reference pitch RAO from the ShipX (VERES) simulation at head sea (left), and the power spectral densities (PSDs) of the measured waves and pitch motions for Test 4020. (For interpretation of the references to color in this figure legend, the reader is referred to the web version of this article.)

loads at different frequencies. This type of phenomenon has been observed, explained, and reported by researchers, e.g., by Rezende et al. [41]. For example, wave components at 6 s and 10 s will lead to a difference-frequency response at a period of 15 s. Motions due to the second-order effects must be excluded from the seakeeping model tuning because only the first-order wave-induced vessel motions are considered in the algorithm. From Fig. 7, the good matching of the VERES-simulated and the measured roll RAOs within the wave frequency ranges indicates that these second-order roll motions are mostly outside the wave frequency range for each individual sea state. Therefore, these second-order motions can be largely excluded by applying a high-pass FFT filter for periods with very small wave energies. For each sea state, the wave and response components at frequencies with wave PSDs less than 5% of the maximum wave PSD value were removed.

In addition, coupling effects between the moonpool piston mode and vessel motions were observed in the case of oblique seas. As illustrated in Fig. 8, the measured heave RAOs based on those test cases with a wave heading of 30° show a second peak at approximately 8 to 9 s, which is significantly different from the VERES-simulated RAO without considering the coupling effects. Similarly, Fig. 9 shows local RAO amplitude peaks at the moonpool piston resonance period for the roll motion at oblique seas (e.g., at 30° and 150°). However, this coupling has significantly less influence for a wave heading of 150° than for 30°, which may be due to the shielding effect from the vessel body on the wave kinematics at the moonpools. The moonpools are located in the vessel forepart. These deviations contribute to the uncertainties of the measurement functions and consequently the predicted measurements. Therefore, the measurement noise matrix $\boldsymbol{R}$ should consider these errors due to simplifications of the seakeeping simulation.

4.2. State space

In practice, the vessel attitude-related parameters, e.g., draft, trim, heel, heading, and forward speed, can be measured by various onboard monitoring systems and hence may be less uncertain. In addition, the vessel geometry can normally be treated deterministically, subject to minor uncertainty due to thorough design and manufacturing work at shipyards. Therefore, within their practical uncertainty ranges, the variation of parameters related to vessel attitude and geometry may have very limited influence on the wave-induced vessel motions. However, due to the frequently shifted vessel loading conditions, potential engineering errors, and considered simplifications and assumptions in the theory, the parameters related to the inertia distribution and hydrodynamic damping may be subject to significant uncertainties.

Similar to [27], the sensitivity of the important uncertain vessel parameters was studied based on the ShipX model, which was deployed during the model testing project. The sensitivity results are qualitatively summarized in Table 3. The RAOs for heave, roll and pitch at the COG are compared within the considered uncertainty range for each uncertain parameter. The influential vessel parameters, i.e., β_{33}, β_{44}, β_{55}, ZCG, r_{44}, and r_{55}, were therefore considered in the system state vector for the model tuning.

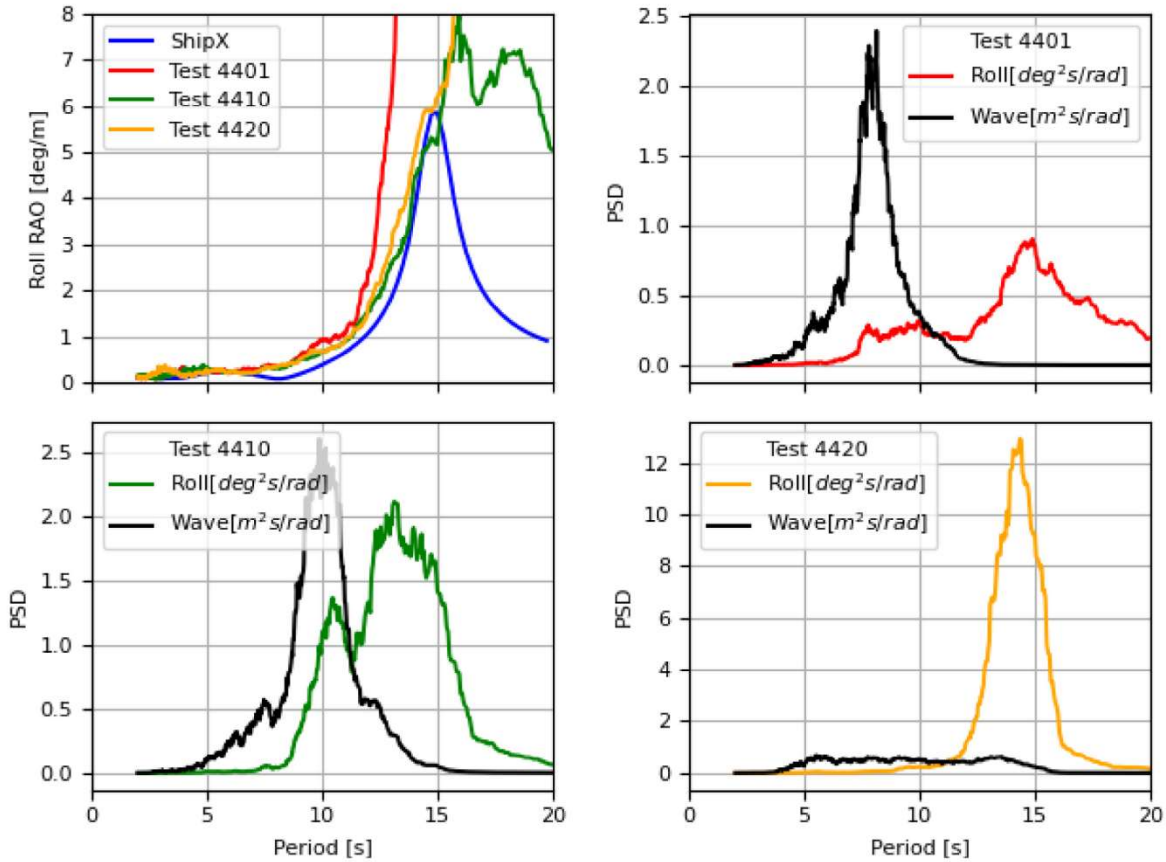

Fig. 7. The measured roll RAOs and the reference roll RAO from the ShipX (VERES) simulation at beam sea (top left), and the power spectral densities (PSDs) of the measured waves and roll motions for Tests 4401, 4410, and 4420. (For interpretation of the references to color in this figure legend, the reader is referred to the web version of this article.)

Table 3
Sensitivity of uncertain vessel parameters.

Parameter	Range	Heave	Roll	Pitch
β_{33}	[0, 10%]	Significant	No	No
β'_{44}	[−7, 7%]	No	Significant	No
β_{55}	[0, 10%]	Minor	No	Significant
ZCG	[6.8, 13.8] m	No	Significant	Minor
r_{44}	[9.5, 11.5] m	No	Significant	No
r_{55}	[41, 49] m	Minor	No	Significant

The linearized additional damping coefficients were assumed constant. The dependency on the sea state characteristics (i.e., H_s, T_p, β_W, etc.) should be considered in practical applications. However, the number of available model tests was limited. Roll motion is most sensitive to the additional damping, particularly around the resonance period. However, the wave peak periods for most tests were 8 s or 10 s, which are outside the resonance; therefore, the additional roll damping plays a very limited role with respect to the measured roll motions. Thus, constant additional damping was believed sufficient for the validation analyses based on these model test cases.

According to Eq. (1), the covariance matrix $\boldsymbol{P}_k$ should be positive semidefinite. Non-negative weight factors w^c guarantee this positive semidefinite property for $\boldsymbol{P}_k$ [24]. However, in practice, it is challenging to have a positive weight factor w_0^c for the state mean $\boldsymbol{\mathcal{X}}_{k+1,0}$ because a very small α is preferred in the algorithm. Non-positive semidefinite $\boldsymbol{P}$ was observed in the initial studies due to the system nonlinearity and the numerical issue caused by too large difference in the order of magnitudes for the diagonal elements of $\boldsymbol{P}$. In addition, when divergent or irrational tuning results occur, unexpected and extremely nonlinear behavior may lead to a non-positive semidefinite covariance matrix. Therefore, the additional damping coefficients (as a percentage) instead of the additional damping and the radii of gyration instead of the moments of inertia are considered in the system state space.

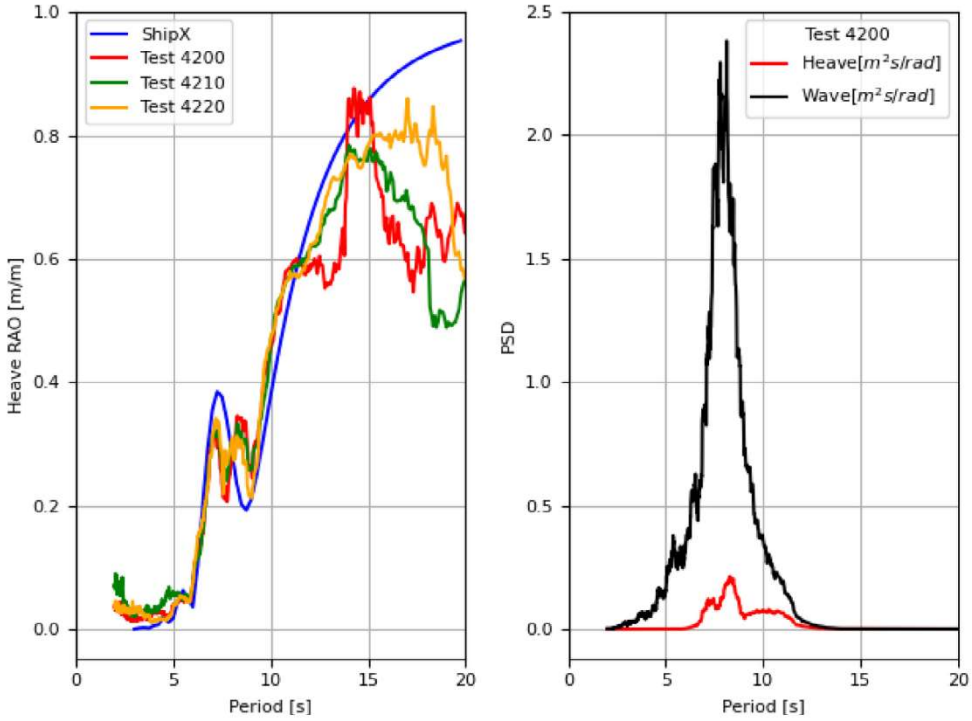

Fig. 8. The measured heave RAO and the reference heave RAO from the ShipX (VERES) simulation for $\beta_W = 30°$ (left), and the power spectral densities (PSDs) of the measured waves and heave motions for Test 4200. (For interpretation of the references to color in this figure legend, the reader is referred to the web version of this article.)

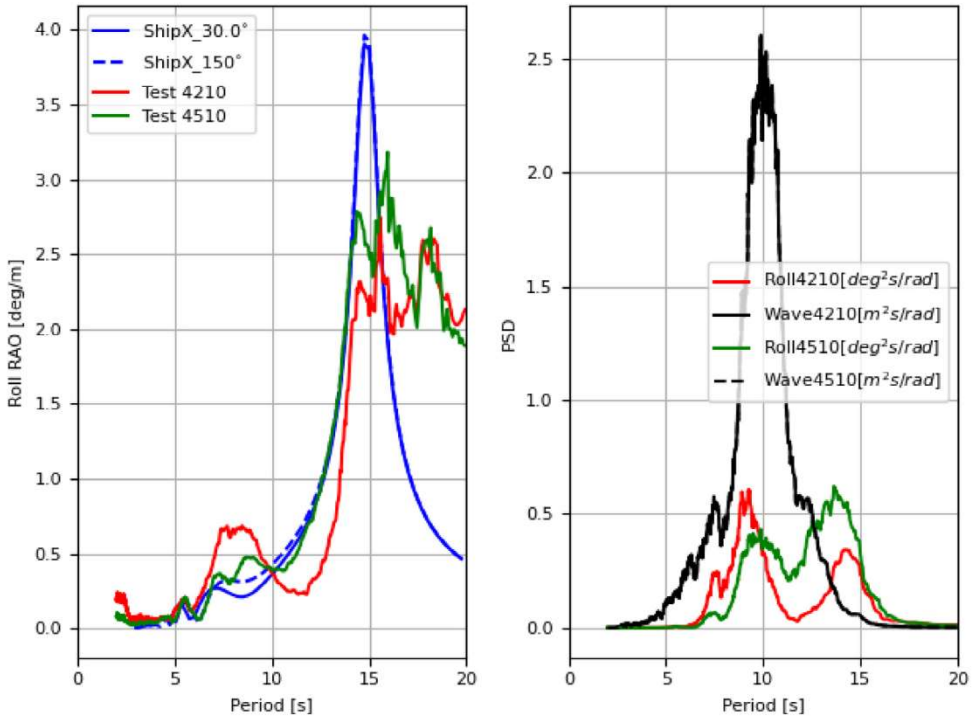

Fig. 9. The measured roll RAOs for Tests 4210 and 4510 and the reference roll RAOs from the ShipX (VERES) simulation for $\beta_W = 30°$and$150°$ (left), and the power spectral densities (PSDs) of the measured waves and roll motions for Tests 4210 and 4510. The wave spectra of Tests 4210 and 4510 are nearly identical. (For interpretation of the references to color in this figure legend, the reader is referred to the web version of this article.)

Table 4
Candidates of diagonal elements of measurement uncertainty variance matrix $\boldsymbol{R}$.

Parameter	Description	Value
$\sigma_N^2(X_3),\ X_3 \in \{\eta_3, \dot{\eta}_3, \ddot{\eta}_3\}$	Noise variance of σ_{X_3} [a]	$\max(2\%\sigma_{X_3}^2, 10^{-6})$
$\sigma_N^2(X_4),\ X_4 \in \{\eta_4, \dot{\eta}_4, \ddot{\eta}_4\}$	Noise variance of σ_{X_4} [b]	$\max(9\%\sigma_{X_4}^2, 10^{-4})$
$\sigma_N^2(X_5),\ X_5 \in \{\eta_5, \dot{\eta}_5, \ddot{\eta}_5\}$	Noise variance of σ_{X_5} [c]	$\max(5\%\sigma_{X_5}^2, 10^{-4})$
$\sigma_N^2(T_z)$	Noise variance of T_z for η_3, η_4, η_5	0.1 s^2 for η_3 and η_5; 0.25 s^2 for η_4

[a] σ_{X_3}: the standard deviation of the heave displacement, velocity, and acceleration measurements.
[b] σ_{X_4}: the standard deviation of the roll rotation, velocity, and acceleration measurements.
[c] σ_{X_5}: the standard deviation of the pitch rotation, velocity, and acceleration measurements.

4.3. Measurement space

One of the keys to success for the tuning process is the selection of the measurement space and the determination of the corresponding errors from measurements (i.e., random errors) and measurement functions (i.e., systematic errors). Initial studies indicate that including derivative information of the measured positions and orientations (i.e., heave, roll and pitch) helps to improve the convergence of the tuning results. However, this applies only if the simulated RAOs based on the true vessel parameters can represent the real responses well. When the reference RAOs are significantly deviated from the true system dynamics, a more informative measurement space (e.g., including the velocity, acceleration, and zero-up-crossing period) for that specific DOF will generally lead to more biased tuning results.

For the model tests, the error sources of the simulated RAOs and the consequent predicted measurements are explained in Section 4.1 and are mainly due to ignoring or linearizing the nonlinear effects and the limitations of linear potential theory and strip theory. Consequently, the measurement uncertainty matrix $\boldsymbol{R}$ has to include these errors and uncertainties. Compared with the measured RAOs, significant errors of the simulated reference RAOs based on the true vessel parameters were observed for the pitch with wave headings between 90° and 180° and all the roll responses. Even more errors were seen for the roll response with wave headings from 0° (not inclusive) to 90° (not inclusive). The measurement space related to the roll motion should therefore be associated with a larger variance in $\boldsymbol{R}$.

For the algorithm to work, note that one fundamental assumption should be fulfilled, i.e., the wave-induced vessel motions can be well represented by the linear transfer functions (RAOs) simulated by the seakeeping analysis. This normally holds for conventional vessels on moderate seas, especially for heave and pitch. The RAOs generated by different software can be different [4,42]. However, benchmarking of the results generated by software in comparison with the results from experiments and onsite measurements has not been extensively performed and published. Comparison studies [4,42] indicate that

(1) The estimated heave and pitch motion RAOs from most seakeeping solvers match each other well, and they are in agreement with experiments.
(2) Strip theory generally overestimates the local trough (i.e., the RAO amplitude at trough is too small) regarding the cancellation effects for pitch and heave at high frequencies.
(3) Much more deviations and uncertainties of the estimated roll motion RAO are often observed when comparing with various seakeeping solvers, and generally none of the programs or theories outperforms the others when benchmarking with experiments.
(4) A deviated estimation of the roll resonance period between programs is often observed.
(5) Largely deviated estimation of the roll RAO amplitudes is observed across all wave periods, partly due to the applied different approaches for viscous damping estimation.
(6) Seakeeping programs based on strip theories perform equally as well (or equally as poorly) as panel-model-based programs.

The vessel position and orientation measured by the OQUS cameras are subject to measurement errors, which should also be considered in $\boldsymbol{R}$, but these are less significant within the main wave frequencies. For the derivative information, the power and the associated noise of the position and orientation measurements are weighted by ω^2 and ω^4 at each frequency according to Eq. (8). The considered range of ω is usually $[0.5, 1.26]$ rad/s. Therefore, the standard deviations of the derived velocity and acceleration are approximately at the same level as that of the (angular) displacement after bandpass filtering of the signals described in Section 3. Consequently, the random errors of those calculated response standard deviations with different derivative orders are also expected to be approximately of the same magnitude for each motion mode.

The diagonal elements in $\boldsymbol{R}$ are summarized in Table 4 with consideration of the aforementioned systematic and measurement errors. The off-diagonal elements of $\boldsymbol{R}$ are all zero. The designed $\boldsymbol{R}$ matrix in Table 4, without optimization, was applied to investigate the UKF-based tuning algorithm performance, which is considered sufficient for demonstration purposes.

For vessel motion measurements with significant energies, the associated measurement uncertainties were assumed to be proportional to the measured response energies. A lower bound value for each $\sigma_N^2(X_d)$ was set mainly to avoid over-confident and biased tuning. For certain combinations of β_W and T_p, some vessel motions can be less significant, e.g., roll motions around head sea outside of roll resonance period. Consequently, the corresponding random and numerical errors will become more predominant in percentage of the associated motion signal energy, compared with the percentage at other wave conditions. Hence, the measurement

Table 5
Parameters applied in Case 1 related to UKF modeling.

Parameter	Value
State space $\boldsymbol{x}$	$\boldsymbol{x} = [\beta_{33}, \beta'_{44}, \beta_{55}, \mathrm{ZCG}, r_{44}, r_{55}]^{\top}$
Initial $\boldsymbol{x}_0$	$\boldsymbol{x}_0 = [2, 2, 2, 10.79, 12, 41]^{\top}$
Initial $\boldsymbol{P}_0$	$\boldsymbol{P}_0 = \mathrm{diag}(25, 64, 25, 0.04, 4, 25)$
$\boldsymbol{Q}$	$\boldsymbol{Q} = \mathrm{diag}(0.25, 0.25, 0.25, 0.05^2, 0.09, 0.25)$
Measurement space $\boldsymbol{z}$	$\boldsymbol{z} = [\sigma_{\eta_3}, \sigma_{\eta_4}, \sigma_{\eta_5}, \sigma_{\dot{\eta}_3}, \sigma_{\dot{\eta}_4}, \sigma_{\dot{\eta}_5}, \sigma_{\ddot{\eta}_3}, \sigma_{\ddot{\eta}_5}, T_{z(\eta_3)}, T_{z(\eta_5)}]$
$\boldsymbol{R}$	Per Table 4
α	0.01
β	2
κ	−3

uncertainties of certain motions may be underestimated at the less critical sea states if the same ratio of the signal energy is applied across different motion energy levels. Therefore, a minimum value for each $\sigma_N^2(X_d)$ was introduced. Considering $\omega \in [0.5, 1.26]$ rad/s and Eqs. (8) and (9), the same lower bound of measurement uncertainties was applied for displacement, velocity, and acceleration of each motion mode, assuming that the response measurement uncertainties at those less critical wave conditions are mostly contributed from random and numerical errors. Design of $\boldsymbol{R}$ can be optimized, but is considered out of the present research scope.

4.4. Validation analysis cases

Based on initial studies of the model tests, numerical simulations, and the important concerns regarding the selection of the state space and measurement space described in Sections 4.1 to 4.3, the scope of the validation analyses is summarized in this section. Four validation analysis cases are included (referred to as Case 1 to Case 4) to demonstrate the performance and limitations of the algorithm. Tables 5 to 8 summarize the UKF modeling for the 4 cases. All the model tests in Table 1 are considered. The differences among the 4 cases are emphasized through the use of underlines.

The applied values of the initial state vector $\boldsymbol{x}_0$, its initial covariance matrix $\boldsymbol{P}_0$, and the process covariance matrix $\boldsymbol{Q}$ are tentative. Selection of the initial state vector $\boldsymbol{x}_0$ and its initial covariance matrix $\boldsymbol{P}_0$ should reflect the relevant prior knowledge in real applications, based on available technical documentation and engineering judgement. In practice, a slightly larger $\boldsymbol{P}_0$ could increase the initial rate of the state tuning towards the true values [22]. After tuning, the convergent state vector should ideally approach the true state while its convergent covariance matrix should basically reflect the uncertainties of the system propagation model, measurement functions, measurement uncertainties, etc. Therefore, the mean vector of the convergent state and the corresponding covariance are ideally independent of their initial choices. However, due to the nonlinear and multimodal characteristics, the tuning is still expected to be dependent on the initialization, especially before asymptotic convergence of the tuning results. The system propagation model, i.e., Eq. (6), assumes a constant system state for all sea states. The process uncertainty $\boldsymbol{Q}$ should reflect the possible variations of the true state across the different tested sea states. In the case studies, the true values of ZCG, r_{44}, and r_{55} remain unchanged while the linearized additional damping terms (i.e., β_{33}, β'_{44}, and β_{55}) are not strictly constant across sea states as explained in Section 4.2. Hence, compared with the process uncertainties of those linearized additional damping terms, relatively small process uncertainties were applied to the terms that are related to the inertia distribution (i.e., ZCG, r_{44}, and r_{55}). In principle, $\boldsymbol{Q}$ should account for possible state variation across different sea states and operational scenarios [22].

The hyperparameters α, β, κ are the same for all cases and are therefore shown only in Table 5. For the seakeeping model parameter tuning, a very small α helps to stabilize the tuning and to capture the important local nonlinear effects. The values of β and κ have less influence on the tuning results. The same parameters are included as the state space in all 4 cases, as described in Section 4.2.

Due to the significant errors of the measurement characteristics between the predicted and the measured described in Section 4.1, it is important to determine the measurement space with extra caution. The standard deviations of η_3, η_5, the first two orders of their derivatives, and their zero-up-crossing periods (T_z) are included in the measurement space for Case 1, considering the fact that the seakeeping analyses normally predict the heave and pitch motions well. However, only roll angular displacement η_4 is included in the measurement space for Case 1 due to (1) the generally less accurate seakeeping simulations; (2) the significant errors due to the ignorance of the moonpool coupling and the second-order motion effects (e.g., Figs. 7 and 9); and (3) the fact that the mean wave loads are outside the roll resonance period.

In Case 2 (Table 6), the measurement space and the measurement noise matrix $\boldsymbol{R}$ are further modified. It was observed that the simulated pitch RAOs were significantly underestimated compared with the measured ones for wave headings between 90° and 180° (e.g., Fig. 10). This result may be caused by the moonpool effects. Therefore, the derivatives and T_z for pitch motion are not included for $\beta_W \geq 90°$ in Case 2. In addition, less measurement noise variance is considered for pitch-related measurements with $\beta_W < 90°$ due to the relatively accurate simulation.

Both Case 1 and Case 2 considered ZCG to be associated with a relatively high confidence, i.e., a standard deviation of 0.2 m, corresponding to ±0.4 m for a 95% confidence interval. Much higher uncertainty of ZCG is considered in Case 3, as shown in Table 7. This case is provided to show the tuning challenges of nonlinear and multimodal systems caused by the interactions of some vessel parameters for the same DOF as well as interactions with multiple DOFs affected by the same vessel parameter.

Compared with Case 2, the measurement space in Case 4 (Table 8) is further modified. Roll motion is not included in the measurement space for $\beta_W < 90°$, while pitch motion is not considered for $\beta_W \geq 90°$.

Table 6
Parameters applied in Case 2 related to UKF modeling. Differences from Case 1 are underlined.

Parameter	Value
State space $\boldsymbol{x}$	$\boldsymbol{x} = [\beta_{33}, \beta'_{44}, \beta_{55}, \mathrm{ZCG}, r_{44}, r_{55}]^\top$
Initial $\boldsymbol{x}_0$	$\boldsymbol{x}_0 = [2, 2, 2, 10.79, 12, 41]^\top$
Initial $\boldsymbol{P}_0$	$\boldsymbol{P}_0 = \mathrm{diag}(25, 64, 25, 0.04, 4, 25)$
$\boldsymbol{Q}$	$\boldsymbol{Q} = \mathrm{diag}(0.25, 0.25, 0.25, 0.05^2, 0.09, 0.25)$
Measurement space $\boldsymbol{z}$	$\beta_W < 90°$: $\boldsymbol{z} = [\sigma_{\eta_3}, \sigma_{\eta_4}, \sigma_{\eta_5}, \sigma_{\dot{\eta}_3}, \sigma_{\dot{\eta}_5}, \sigma_{\ddot{\eta}_3}, \sigma_{\ddot{\eta}_5}, T_{z(\eta_3)}, T_{z(\eta_5)}]$ $\beta_W \geq 90°$: $\boldsymbol{z} = [\sigma_{\eta_3}, \sigma_{\eta_4}, \sigma_{\eta_5}, \sigma_{\dot{\eta}_3}, \sigma_{\ddot{\eta}_3}, T_{z(\eta_3)}]$
$\boldsymbol{R}$	σ_{X_5} for $\beta_W < 90°$: $\max(\underline{2\%}\sigma^2_{X_5}, 10^{-4})$; otherwise: Per Table 4

Table 7
Parameters applied in Case 3 related to UKF modeling. Differences from Case 2 are underlined.

Parameter	Value
State space $\boldsymbol{x}$	$\boldsymbol{x} = [\beta_{33}, \beta'_{44}, \beta_{55}, \mathrm{ZCG}, r_{44}, r_{55}]^\top$
Initial $\boldsymbol{x}_0$	$\boldsymbol{x}_0 = [2, 2, 2, \underline{11.5}, 12, 41]^\top$
Initial $\boldsymbol{P}_0$	$\boldsymbol{P}_0 = \mathrm{diag}(25, 64, 25, \underline{1.0}, 4, 25)$
$\boldsymbol{Q}$	$\boldsymbol{Q} = \mathrm{diag}(0.25, 0.25, 0.25, 0.05^2, 0.09, 0.25)$
Measurement space $\boldsymbol{z}$	Per Case 2 (Table 6)
$\boldsymbol{R}$	Per Case 2 (Table 6)

Table 8
Parameters applied in Case 4 related to UKF modeling. Differences from Case 2 are underlined.

Parameter	Value
State space $\boldsymbol{x}$	$\boldsymbol{x} = [\beta_{33}, \beta'_{44}, \beta_{55}, \mathrm{ZCG}, r_{44}, r_{55}]^\top$
Initial $\boldsymbol{x}_0$	$\boldsymbol{x}_0 = [2, 2, 2, 10.79, 12, 41]^\top$
Initial $\boldsymbol{P}_0$	$\boldsymbol{P}_0 = \mathrm{diag}(25, 64, 25, 0.04, 4, 25)$
$\boldsymbol{Q}$	$\boldsymbol{Q} = \mathrm{diag}(0.25, 0.25, 0.25, 0.05^2, 0.09, 0.25)$
Measurement space $\boldsymbol{z}$	$\beta_W < 90°$: $\boldsymbol{z} = [\sigma_{\eta_3}, \sigma_{\eta_5}, \sigma_{\dot{\eta}_3}, \sigma_{\dot{\eta}_5}, \sigma_{\ddot{\eta}_3}, \sigma_{\ddot{\eta}_5}, T_{z(\eta_3)}, T_{z(\eta_5)}]$ $\beta_W \geq 90°$: $\boldsymbol{z} = [\sigma_{\eta_3}, \sigma_{\eta_4}, \sigma_{\dot{\eta}_3}, \sigma_{\ddot{\eta}_3}, T_{z(\eta_3)}]$
$\boldsymbol{R}$	Per Case 2 (Table 6)

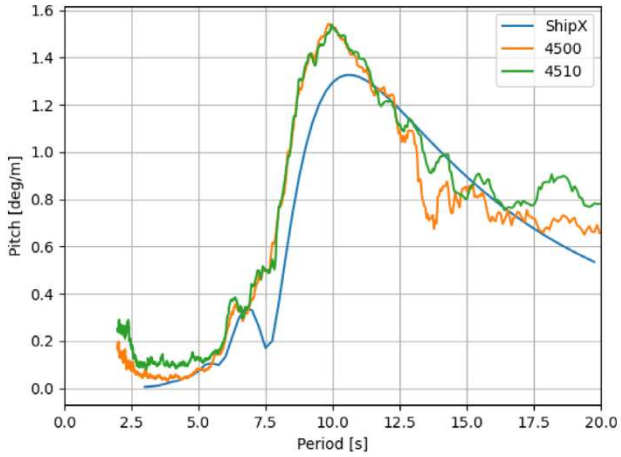

Fig. 10. The reference pitch RAO from the ShipX (VERES) simulation and the measured pitch RAOs based on Tests 4500 and 4510 for a wave heading of 150°. (For interpretation of the references to color in this figure legend, the reader is referred to the web version of this article.)

5. Results

The tuning results from the 4 cases described in Section 4.4 are summarized, discussed, and compared in this section. The objectives of the tuning are not only to improve the vessel motion estimation at the present tuning sea state but much more importantly to improve the knowledge regarding the uncertain vessel parameters to achieve more accurate RAOs for better vessel motion prediction in relation to future unobserved sea states, especially for the most critical wave conditions. For convenience of discussion, the true values of the uncertain vessel parameters are denoted by $\boldsymbol{x}^* = [\beta^*_{33}, \beta'^*_{44}, \beta^*_{55}, \mathrm{ZCG}^*, r^*_{44}, r^*_{55}]^\top = [0, 0, 0, 10.82, 10.5, 44.8]^\top$.

It is worth mentioning that the proposed tuning algorithm is computationally very efficient for large-dimensional nonlinear systems. For the case studies with a 6-dimensional state vector and the seakeeping simulation by ShipX (VERES), the validation analysis took less than 2 h to tune through all 24 test cases in Table 1 when running 7 VERES analyses in parallel, i.e., less than 5 min per model test case. The time spent was dominated by the seakeeping simulations. Having completed the seakeeping simulations, the tuning for each model test case took approximately 3 s.

5.1. Case 1

The tuning of the uncertain vessel parameters for Case 1 is shown in Fig. 11. The "Predicted" lines in black indicate the prediction of those parameters after the system propagation step corresponding to Eq. (6), and the filled gray areas illustrate their 95% confidence intervals (i.e., $\pm 2\sigma$ for Gaussian variables). The "Updated" lines in red indicate the updated estimation of those uncertain vessel parameters after the measurement update step corresponding to Eqs. (7)–(13), and the filled red areas illustrate their 95% confidence intervals. The dashed lines in green indicate the corresponding true values specified in the model tests. For the additional damping terms, true values are not available.

As illustrated in Fig. 11a, β_{33} varies around zero, as expected. The negative β_{33} for the following sea conditions ($k > 17$) suggests a possible underestimation of the heave responses from the VERES simulation at the relevant wave conditions. The heave resonance is at approximately 6 to 9 s, where significant wave loads are present in the model tests. Referring to Table 3, only β_{33} in the system state can significantly influence the heave RAO amplitude around the periods of interest. A greatly reduced uncertainty of β_{33} is also shown in Fig. 11a.

The peak of the pitch RAO also occurs at approximately 7 to 10 s. Therefore, β_{55} is expected to have a significant influence on the pitch response for the tested wave conditions. For $\beta_W < 90°$, β_{55} was quickly tuned to 0%, while r_{55} (Fig. 11f) gradually approached its true value. This suggests that the VERES-simulated pitch RAOs based on the true value of r_{55} without additional damping match the measurements very well, as shown in Fig. 6. However, for $\beta_W < 90°$, a dramatic decrease in β_{55} and increase in r_{55} are observed, both leading to an increase in the pitch motions for the tested wave conditions. This outcome also reveals the deviation in the pitch estimation by the ShipX (VERES) simulations based on the true r_{55} and zero β_{55} for $\beta_W \geq 90°$, e.g., as shown in Fig. 10. Even though the tuned r_{55} in Case 1 largely deviated from the true value when $k > 15$, in fact, the corresponding pitch estimations for those testing wave conditions were significantly improved. For example, Fig. 12 compares the pitch motion spectra estimated based on the true vessel parameters $\boldsymbol{x}^*$ (blue), the tuned vessel parameters $\boldsymbol{x}_{19}$ (orange), and the measurements (green). It is obvious that the tuned state vector $\boldsymbol{x}_{19}$ significantly improves the estimation accuracy of pitch motion at the wave condition for Test 4510, which is also supported by the improved pitch RAO at $\beta_W = 150°$, as shown in Fig. 13. However, this may not help in the prediction of pitch motion for other wave conditions. The VERES-simulated pitch RAO at head sea $\beta_W = 0°$ after tuning for Test 4510 is illustrated in Fig. 14. In comparison with the pitch RAOs based on $\boldsymbol{x}^*$ and the measurements from the relevant test cases, the simulated RAO after tuning for Test 4510 deviates significantly, leading to increased prediction errors for head seas.

For the tuning of roll-related parameters, very little change in β'_{44} and its uncertainty is observed in Fig. 11b because the roll resonance period is approximately 15 s, where little wave energy exists for almost all the test cases. The damping term has a very limited effect on the responses outside the resonance. ZCG also changed less significantly due to its relatively small uncertainty. The uncertainty of ZCG even increased, as shown in Fig. 11d, indicating an initial underestimation of the uncertainty. A slightly deviating tuning of r_{44} is shown in Fig. 11e. As pointed out in Section 4.4, software-induced errors are most onerous in the roll motion estimation, and therefore, biased tuning for parameters related to roll motion is very challenging to handle. Indeed, a much more severe tuning bias of r_{44} can be obtained when the measurement space includes the derivatives and T_z of the roll angular displacement. It is therefore important to determine the measurement space and the noise matrix.

5.2. Case 2

Compared with Case 1, the measurement space was modified in Case 2, as shown in Table 6: (1) the noise variances of the pitch motion, velocity, and acceleration were reduced from 5% to 2% of the corresponding measured pitch responses for $\beta_W < 90°$; and (2) only the standard deviation of the pitch angular displacement was included in the measurement space with a noise variance of 5%. Fig. 15 illustrates the corresponding tuning results for the 6 uncertain vessel parameters. Compared with Case 1 (Fig. 11), the modification of the measurement space for pitch responses leads to a significant improvement in the tuning of r_{55} (Fig. 15f). Due to the reduction in $\boldsymbol{R}$ for pitch-related measurements for $\beta_W < 90°$ and the fact that the reference pitch RAO based on $\boldsymbol{x}^*$ matches very well with the measurements for $\beta_W < 90°$, faster tuning convergence of r_{55} was observed for Case 2. Furthermore, because the pitch motion derivatives and T_z were removed from the measurement space for $\beta_W \geq 90°$, the resulting tuned r_{55} value at $k = 24$ deviated much less from the true value, even though the system still intended to increase the value of r_{55}.

On the other hand, worse tuning of β'_{44} (Fig. 15b) and r_{44} (Fig. 15e) were observed, although the measurement space related to roll motion did not change compared with Case 1. This outcome was mainly due to the multimodal and nonlinear characteristics of the seakeeping model tuning problem. Multiple combinations of β'_{44}, ZCG, and r_{44} can possibly lead to the same standard deviation of the roll motion considered in the measurement space. Therefore, the weighted statistical linear regression [26] based on the deterministically selected sigma points may lead to different tuning directions, depending on the state mean, covariance matrix, and hyperparameters of the UKF model. For example, after the system propagation for $k = 7$ (Test 4120), a smaller ZCG and larger r_{44} than in Case 1 were predicted. Different sets of sigma points were therefore assessed between Case 1 and Case 2. A smaller r_{44} helps to reduce the roll resonance period and consequently increase the RAO amplitudes for periods less than the resonance period,

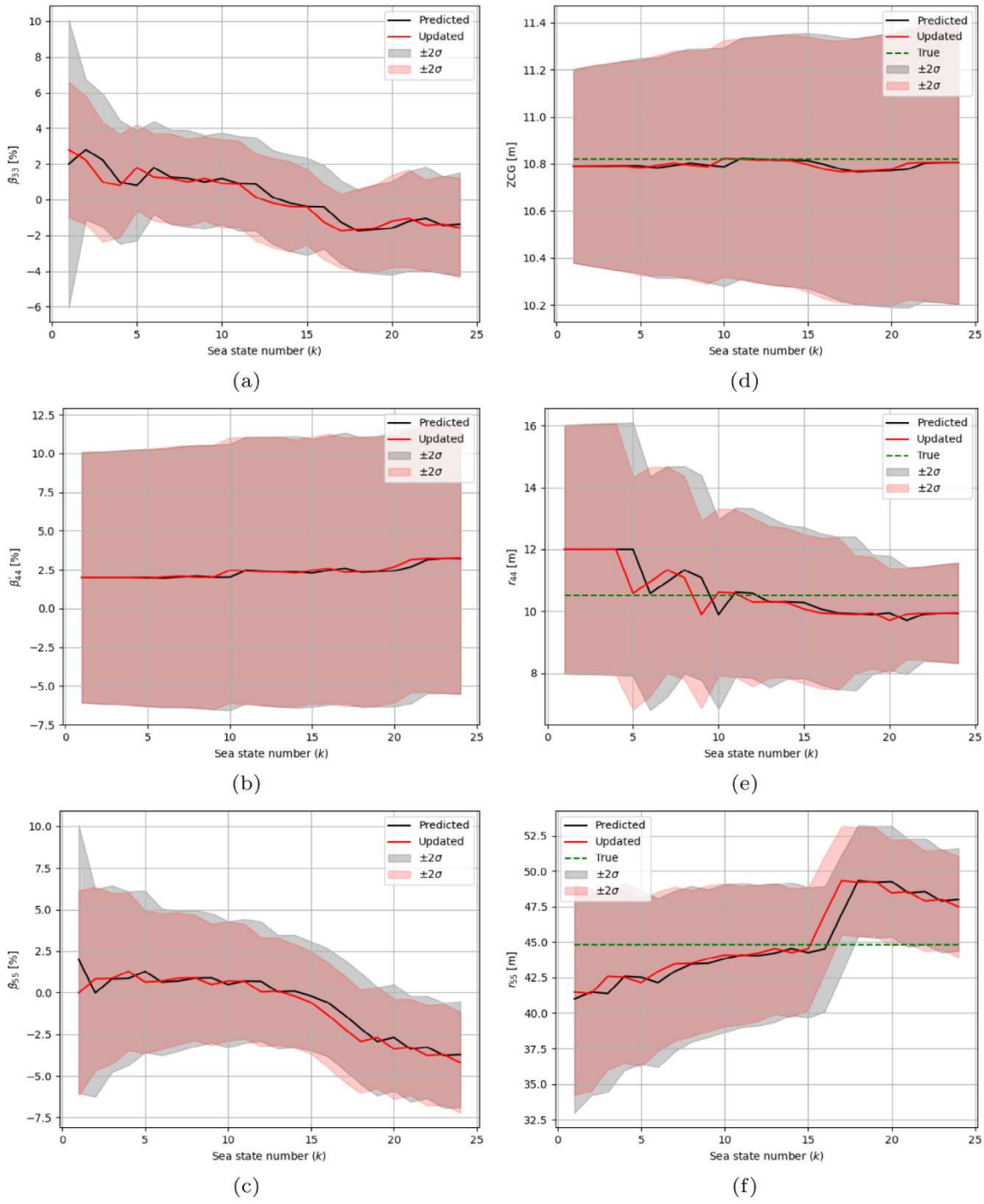

Fig. 11. The state estimation for Case 1 after system propagation ("Predicted") and measurement update ("Updated") for each model test case described in Table 1. Subplots illustrate the tuning of (a) β_{33}; (b) β'_{44}; (c) β_{55}; (d) ZCG; (e) r_{44}; (f) r_{55}. (For interpretation of the references to color in this figure legend, the reader is referred to the web version of this article.)

whereas a larger ZCG stretches the RAO towards larger periods, leading to an increased resonance period, larger RAO amplitudes for small periods (e.g., 3–6 s) before the cancellation effect (e.g., at approximately 8 s in Fig. 7), but smaller RAO amplitudes for larger periods (e.g., 8–14 s) on the lower side of the resonance period. These complicated influences on the roll motions cause the seakeeping parameter tuning to be nonlinear and multimodal, leading to the state-dependent tuning direction. In addition, as

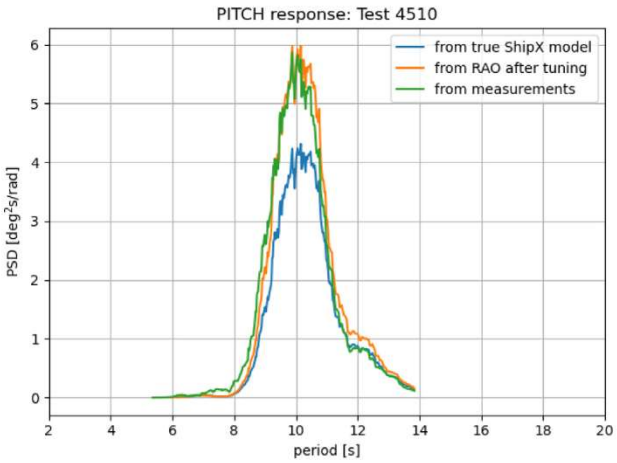

Fig. 12. The pitch motion spectra for the wave condition of Test 4510 ($k = 19$) for $\beta_W = 150°$. Blue: spectrum estimated from the simulated reference RAO based on $\boldsymbol{x}^*$; orange: spectrum estimated from the VERES-simulated RAO based on $\boldsymbol{x}_{19}$; green: spectrum estimated directly from the measurements. (For interpretation of the references to color in this figure legend, the reader is referred to the web version of this article.)

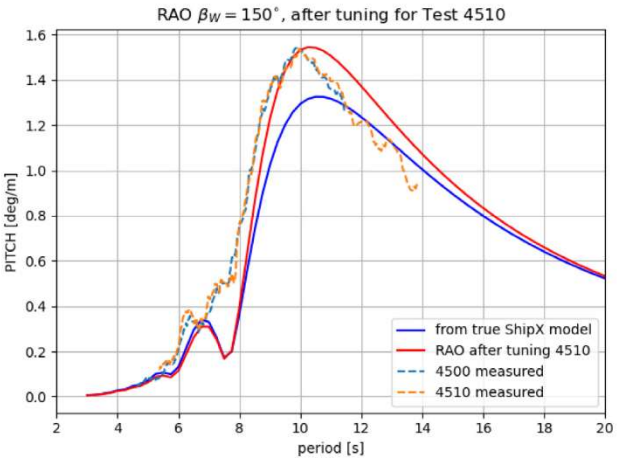

Fig. 13. The pitch RAOs for $\beta_W = 150°$. Blue: the simulated reference RAO based on $\boldsymbol{x}^*$; red: the VERES-simulated RAO based on $\boldsymbol{x}_{19}$, i.e., after tuning for Test 4510 ($k = 19$); dashed: RAOs estimated directly from the measurements for $\beta_W = 150°$. (For interpretation of the references to color in this figure legend, the reader is referred to the web version of this article.)

shown in Fig. 9, a much larger roll motion estimation error is expected for $\beta_W < 90°$ due to the moonpool effects. The high local peak of the roll RAO in Test 4210 (Fig. 9) before 10 s can never be simulated within the considered uncertainty ranges of the parameters and without considering the moonpool coupling effect in the seakeeping simulations. Therefore, reliable tuning of the roll-motion-related parameters cannot be expected for $\beta_W < 90°$.

Compared with Case 1, different tuning results for roll-motion-related parameters were observed for $\beta_W < 90°$ even though the roll-related measurement space is the same for both Case 1 and Case 2 (for $\beta_W < 90°$). This is believed to be due to the small influence of ZCG on the pitch motion as indicated in Table 3. Compared with Case 1, the reduced measurement uncertainty variances ($\boldsymbol{R}$) in Case 2 for pitch-related characteristics at $\beta_W < 90°$ may make the tuning of ZCG more dependent on the pitch measurements. Consequently, the tuning of other roll-motion-related parameters such as β'_{44} and r_{44} can be influenced by those differently tuned ZCG values.

5.3. Case 3

Compared with Case 2, Case 3 changes only the initial value of ZCG and increases the initial variance from 0.04 to 1.0 m^2. The tuning results illustrated in Fig. 16 indicate how the interaction between the tuning of ZCG and that of r_{44} leads to the increasingly biased tuning of r_{44}. Larger ZCG uncertainty allows the UKF model to vary more in terms of the ZCG value to help further reduce the measurement residual. Consequently, biased tuning of the seakeeping model parameters is more likely to occur when the measurement function has significant systematic errors.

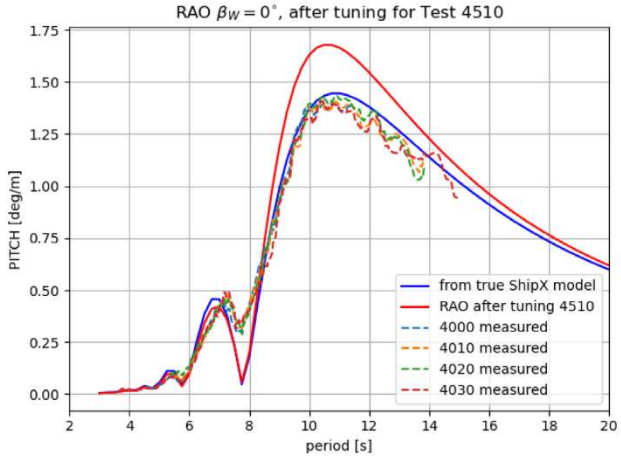

Fig. 14. The pitch RAOs for $\beta_W = 0°$. Blue: the simulated reference RAO based on $\boldsymbol{x}^*$; red: the VERES-simulated RAO based on $\boldsymbol{x}_{19}$, i.e., after tuning for Test 4510 ($k = 19$); dashed: RAOs estimated directly from the measurements for $\beta_W = 0°$. (For interpretation of the references to color in this figure legend, the reader is referred to the web version of this article.)

As shown in Fig. 17, the UKF model succeeded in reducing the residual of the roll motion standard deviation for Test 4420 ($k = 17$) by reducing ZCG (Fig. 16d). Reduced errors in the roll RAOs between those measured (dashed lines) and those simulated by ShipX (VERES) based on $\boldsymbol{x}_{17}$ (red) were also observed for periods less than the resonance period, as illustrated in Fig. 18, in comparison with the VERES-simulated RAO based on the true state $\boldsymbol{x}^*$ (blue). However, this updated roll RAO will lead to significant roll motion prediction errors for wave conditions with periods near or larger than the resonance period.

It is also noted that β'_{44} was slightly reduced. In fact, a further reduction in β'_{44} can help to increase the roll spectral density near the resonance (e.g., 13–17 s). However, the linear regression at the selected sigma points for $k = 17$ suggested that tuning ZCG was more efficient, mainly because most of the roll motion energy considered in the measurement space was outside the resonance period, implying a smaller contribution from β'_{44} to the roll motion for this sea state. When calculating the roll motion standard deviation for Test 4420, the spectrum was cut off at a period of 15 s as described in Section 4.1. It is believed that including responses larger than 15 s can help the UKF model realize the contribution of β'_{44} to the roll motion, though only if the second-order roll motion can be clearly removed before tuning. For Test 4420, it is possible that the response periods of the first-order and second-order roll motions overlap due to the broadband wave spectrum. The significant wave loads at 5 to 10 s may induce the second-order roll motions at 10 to 15 s, where significant first-order motions exist. The signal filtering described in Section 4.1 cannot deal with this overlap, leading to additional error sources between the predicted response versus the measured one.

5.4. Case 4

As shown in the previous case studies, biased tuning of r_{44} and r_{55} is due to the systematic errors of the measurement functions introduced by the simulated RAOs $|H_X(\omega, \beta_W|\mathcal{X}_{k+1,i})|$ at the sigma points in Eq. (10). It is assumed in Case 4 that better prior knowledge about the uncertainties of the simulated RAOs can be included, i.e., better matches for (1) the simulated roll RAOs versus the measurement at $\beta_W \geq 90°$ and (2) the simulated pitch RAOs versus the measurement at $\beta_W < 90°$. Therefore, as summarized in Table 8, the measurement space of Case 4 did not consider roll motions for $\beta_W < 90°$ and pitch motions for $\beta_W \geq 90°$.

Fig. 19 illustrates improved tuning results for β_{55} (Fig. 19c), r_{44} (Fig. 19e), and r_{55} (Fig. 19f) compared with those in Case 2. Slightly biased tuning of ZCG is shown in Fig. 19d, mainly due to the significant systematic error in the simulated roll RAOs, even though this error was much less for $\beta_W \geq 90°$.

Comparing Figs. 15f and 19f, it is interesting to note the different tuning r_{55} for $\beta_W < 90°$, e.g., $k \in [6, 14]$, even though the initial state and the measurement space related to pitch motions are the same for Case 2 and Case 4 for $\beta_W < 90°$. In fact, the state covariance matrix $\boldsymbol{P}$ and the matrix square root calculation of $\left[\sqrt{(N+\lambda)\boldsymbol{P}_k}\right]_j$ in Eq. (1) were influenced by removing the roll motion from the measurement space for $\beta_W < 90°$. Consequently, the selection of sigma points and the weighted statistical linear regression were affected, which can easily lead to different tuning results involving nonlinear functions.

Moreover, r_{55} was actively tuned in Case 4 even for $\beta_W > 90°$, where the pitch motions were removed from the measurement space. In fact, the tuning of r_{55} was actually influenced by the heave measurements made at the OQUS camera location, where the heave motion was affected by the coupling effect from the pitch, as shown in Eq. (11). Thus, the pitch-related measurements were implicitly considered in the measurement space for $\beta_W \geq 90°$.

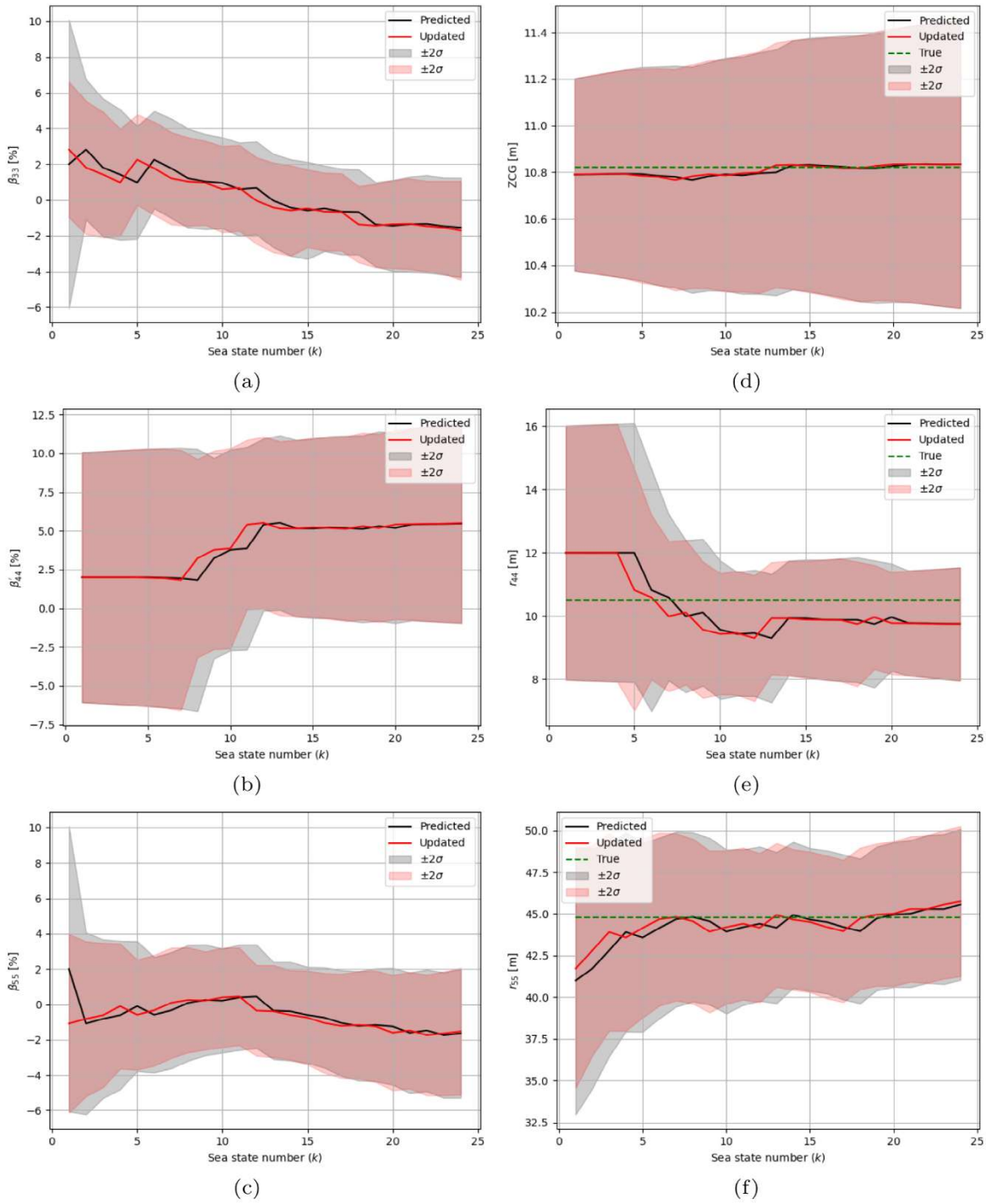

Fig. 15. The state estimation for Case 2 after system propagation ("Predicted") and measurement update ("Updated") for each model test case described in Table 1. Subplots illustrate the tuning of (a) β_{33}; (b) β'_{44}; (c) β_{55}; (d) ZCG; (e) r_{44}; (f) r_{55}. (For interpretation of the references to color in this figure legend, the reader is referred to the web version of this article.)

6. Conclusions and future work

The present paper demonstrated the application of the previously proposed algorithm in relation to the tuning of important uncertain vessel seakeeping parameters based on the unscented Kalman filter (UKF) [22] by using seakeeping (zero speed) model

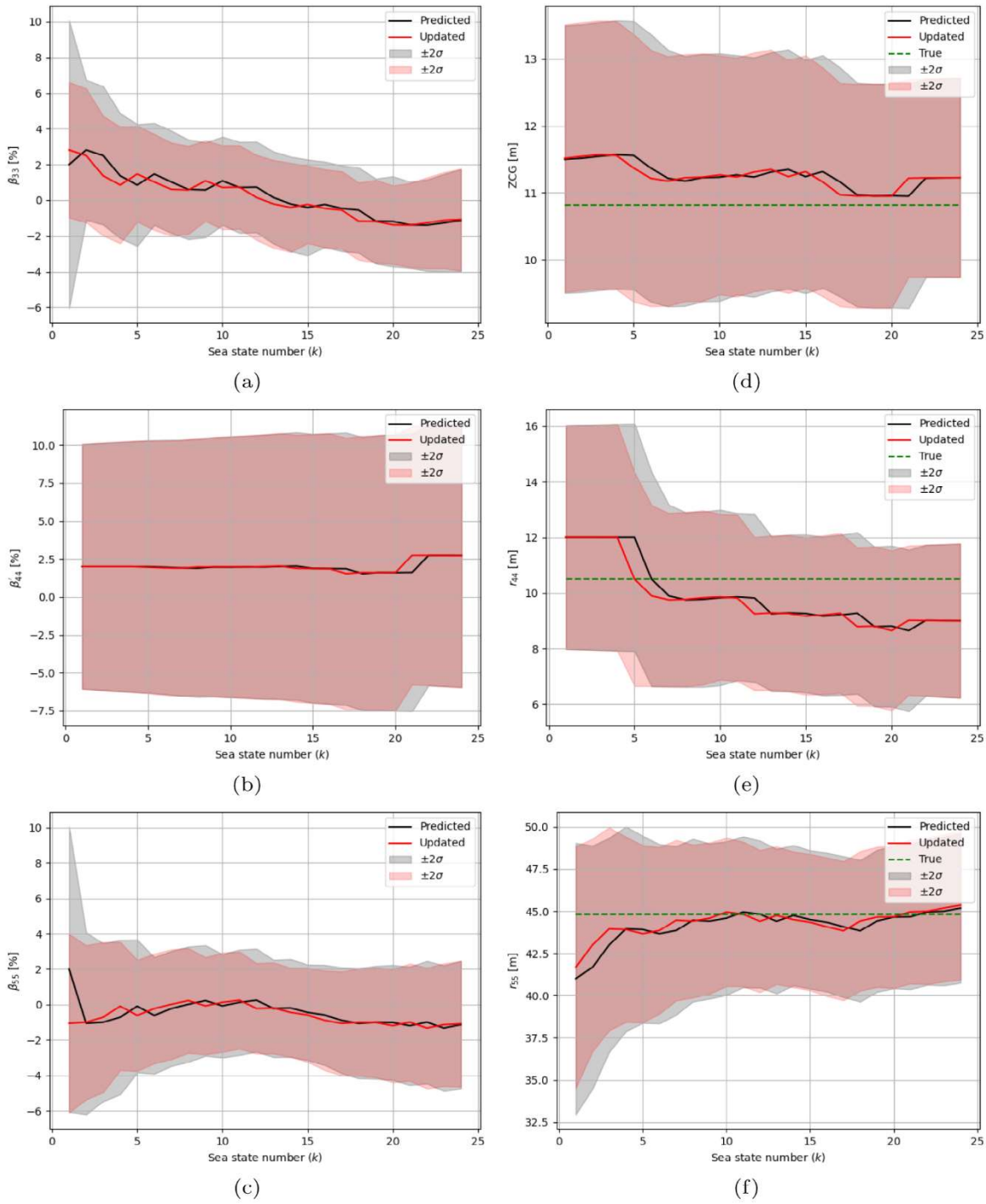

Fig. 16. The state estimation for Case 3 after system propagation ("Predicted") and measurement update ("Updated") for each model test case described in Table 1. Subplots illustrate the tuning of (a) β_{33}; (b) β'_{44}; (c) β_{55}; (d) ZCG; (e) r_{44}; (f) r_{55}. (For interpretation of the references to color in this figure legend, the reader is referred to the web version of this article.)

tests for an advanced offshore construction vessel. The uncertain vessel parameters (i.e., the state space) were selected based on parametric sensitivity studies. Rational tuning results were achieved by carefully designing the measurement space. The influences of the considered state space and measurement space on the tuning results were discussed in Section 5.

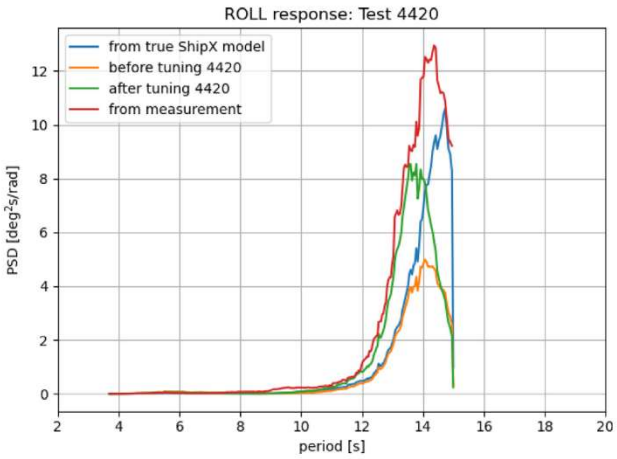

Fig. 17. The roll motion spectra for the wave condition of Test 4420 ($k = 17$). Blue: spectrum estimated from the VERES-simulated RAO based on $\boldsymbol{x}^*$; orange: spectrum estimated from the VERES-simulated RAO based on the state before tuning for Test 4420, i.e., $\boldsymbol{x}_{16}$; green: spectrum estimated from the VERES-simulated RAO based on the state after tuning for Test 4420, i.e., $\boldsymbol{x}_{17}$; red: spectrum estimated directly from the measurements for Test 4420. (For interpretation of the references to color in this figure legend, the reader is referred to the web version of this article.)

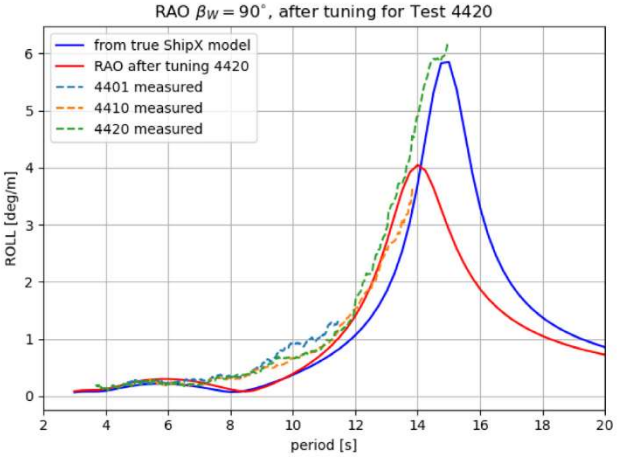

Fig. 18. The roll RAOs for $\beta_W = 90°$. Blue: the VERES-simulated RAO based on $\boldsymbol{x}^*$; red: the VERES-simulated RAO based on $\boldsymbol{x}_{17}$, i.e., after tuning for Test 4420 ($k = 17$); dashed: RAOs estimated directly from the measurements for $\beta_W = 90°$. (For interpretation of the references to color in this figure legend, the reader is referred to the web version of this article.)

The fundamental goal is to modify the important vessel parameters based on vessel motion measurements and the corresponding wave information for a limited number of sea states. Consequently, the accuracy of the calculated linear transfer functions can be improved across the whole range of wave frequencies, particularly at critical frequencies (e.g., around resonance) which may have not been observed. Hence, the most fundamental assumption (and the most critical limitation) is that the linear transfer functions simulated by the application of seakeeping analysis must be sufficiently representative with respect to the relevant vessel motions of interest at the wave frequencies. However, systematic errors are never expected to vanish.

Therefore, it is extremely important to determine the state space and measurement space for a successful tuning. Without inclusion of all the important and uncertain vessel parameters in the state space, the algorithm will try to tune some other influential parameters in the state space to reduce the residual, which will definitely lead to biased tuning results. Understanding the systematic errors from the measurement functions due to the applied simplifications and assumptions associated with the seakeeping simulations and the consequent motion estimation is the key to properly determining the measurement space and its uncertainties. When the systematic errors from seakeeping simulation are relatively small, more relevant measured response characteristics in the measurement space and reduced measurement noise variance can help accelerate the tuning towards the correct values, e.g., the tuning of r_{55} for $\beta_W < 90°$ in Case 2 (Section 5.2). Including characteristics of the response velocities and accelerations into the measurement space can enable tuning towards the true results because the motion PSDs are "weighted" differently at different frequencies. The measurement space is hence more informative.

However, it is advised not to design a too informative measurement space by including excessive measured response characteristics when the systematic errors from the measurement functions are large and especially if they are biased. For example as observed

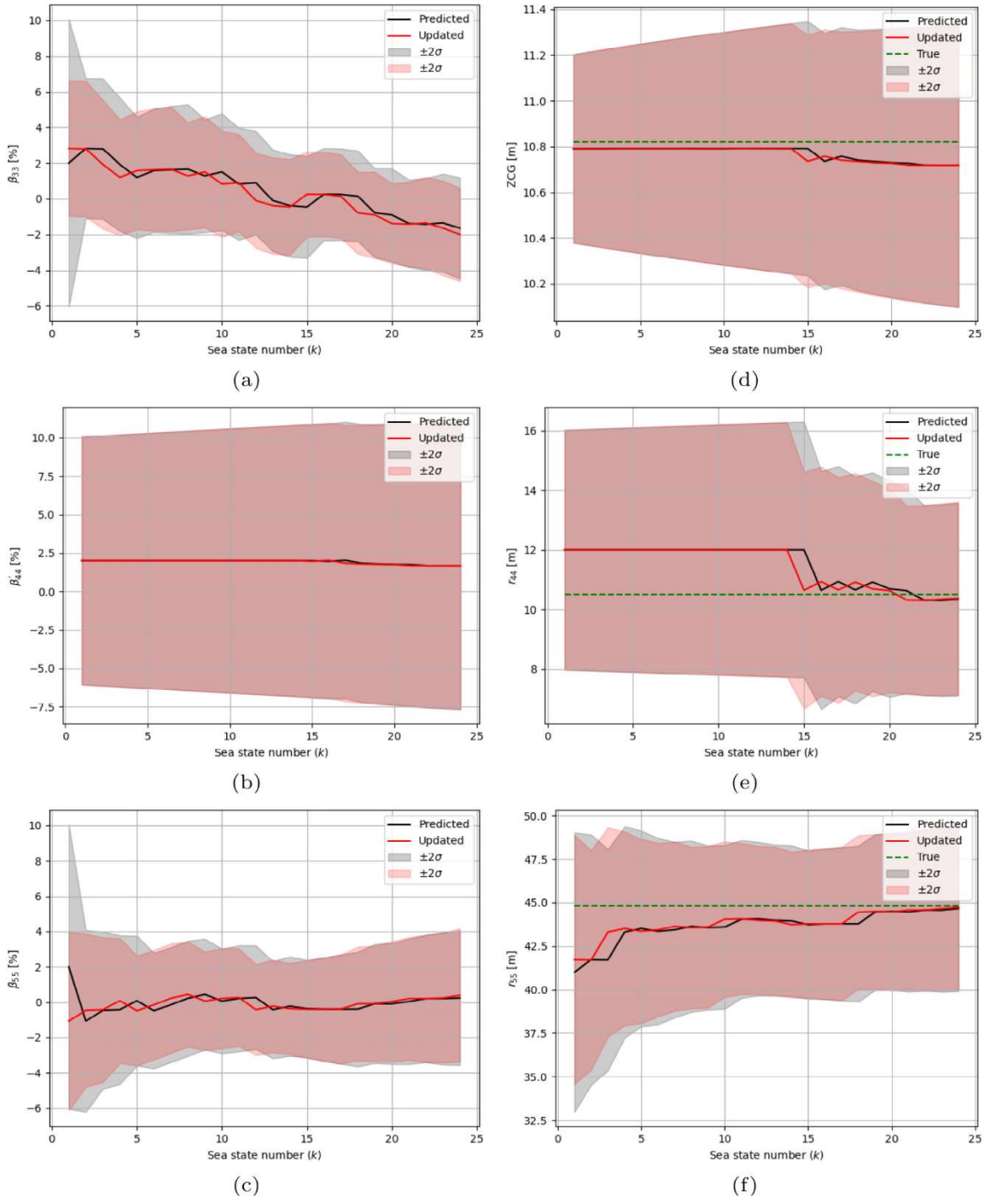

Fig. 19. The state estimation for Case 4 after system propagation ("Predicted") and measurement update ("Updated") for each model test case described in Table 1. Subplots illustrate the tuning of (a) β_{33}; (b) β'_{44}; (c) β_{55}; (d) ZCG; (e) r_{44}; (f) r_{55}. (For interpretation of the references to color in this figure legend, the reader is referred to the web version of this article.)

by a comparison of Figs. 11f and 15f, due to large systematic errors of the reference RAO for pitch with $\beta_W \geq 90°$, the excessive pitch-related measurement space in Case 1 leads to a significantly biased tuning of r_{55}. The existence of moonpools on the studied vessel leads to larger and biased errors of the simulated RAOs for some DOFs at some wave headings, as thoroughly discussed in Section 4.1. Thus, a flexible measurement space that can be modified according to the wave information and improved knowledge on the limitations of the applied seakeeping analysis can potentially improve the tuning results, e.g., as shown in Section 5.4.

All the four cases indicate insignificantly reduced uncertainties of roll-related parameters, i.e., β'_{44}, ZCG, and r_{44}. Even increased uncertainties of β'_{44} (Fig. 16d) and ZCG (Figs. 11d, 15d and 19d) were observed. These observed large uncertainties after tuning are mainly because:

(1) Relatively large measurement uncertainties were applied to the quantities related to roll motion (i.e., σ_{η_4} and $T_{z(\eta_4)}$), as specified in Table 4.
(2) Roll velocity and acceleration were not considered to be part of the measurement space. This less informative roll-related measurement space led to larger uncertainties after convergence.
(3) β'_{44} is basically little sensitive to roll motions for most of the tested sea states, due to the wave spectral peak periods located well away from the roll resonance period.

The increased uncertainty of ZCG for Case 1, Case 2, and Case 4 is believed to be due to its too small initial variance compared with the actual uncertainties from signals, measurement functions, and system propagation model, etc. The convergent variances of those roll-related parameters are actually affected in an interactive way. A less uncertain ZCG led to a less uncertain r_{44} (Figs. 11 and 15), and vice versa (Fig. 16). The resulting large variances of roll-related parameters after tuning are still believed to be very valuable, because:

(a) As long as the estimated uncertainty reflects reality, a model tuning algorithm which provides uncertainty quantification is usually better than parametric optimization algorithms that are based on minimization of a residual (i.e., cost function), which rather results in "deterministic" tuning results. Such deterministic results do not reveal the associated uncertainties and may therefore introduce large estimation errors without this being apparent.
(b) Uncertainty quantification of the important vessel parameters offers a unique opportunity to perform quantitative reliability or risk assessment for advanced onboard decision support systems, in applications related to marine operations, autonomous ships, etc.

Several parameters may influence the same vessel motion in a similar way, e.g., the effect of r_{44} and ZCG on roll motions. Due to the nonlinear and nonmonotonic relationship between the vessel parameters and the characteristics of the relevant measured vessel response, the present algorithm may lead to tuning of the parameters towards wrong values. This may still be acceptable with respect to vessel motion prediction for similar wave conditions but is unacceptable for very different wave conditions. Examples are illustrated in Figs. 14 and 18. Future research needs to clarify how to treat these challenges. The proposed algorithm will in any case try to tune the parameters to reduce the measurement residual, based on assessments at several deterministically selected sigma points around the state mean. Therefore, the tuning is sensitive to the state mean, the state covariance, and the hyperparameters of the UKF model (e.g., α). The algorithm should be further developed to improve its stability and robustness, especially when a critically large bias due to the measurement functions or the system propagation functions exists.

As explained in Section 5.3, the higher-order responses may not be easy to filter out due to the potential overlapping of the response frequency ranges with the first-order responses. Future research is hence required with respect to improving the higher-order response identification and filtering to improve the performance of the tuning algorithm.

In the present paper, the tuning algorithm was assessed only by model-scale measurements in a laboratory environment with minor uncertainties regarding the wave conditions. The tuning algorithm should be further validated by cases involving full-scale measurements, where the uncertainties of sea states are much more significant and therefore must be considered in a probabilistic way, e.g., as proposed by Han et al. [22]. In addition, larger variation in the wave conditions can be expected in real applications. Consequently, the UKF-based tuning algorithm must be modified to tune the sea-state-dependent parameters (e.g., β_{44}) and to use this tuned information in the present sea state to improve the vessel motion prediction accuracy for future unobserved wave conditions.

Declaration of competing interest

The authors declare that they have no known competing financial interests or personal relationships that could have appeared to influence the work reported in this paper.

Acknowledgments

This work was made possible through the Centre for Research based Innovation MOVE, financially supported by the Research Council of Norway, NFR project no. 237929, and the consortium partners (http://www.ntnu.edu/move). Special thanks are given to Salt Ship Design AS for the permission to use the relevant information, data, and numerical model from their seakeeping model tests. Thanks are also given to professor Trygve Kristiansen at NTNU, Martin Gutsch, Senthuran Ravinthrakumar, and Kjetil Berget at SINTEF Ocean AS for the valuable support and discussions regarding model testing, vessel hydrodynamics and moonpool coupling effects.

References

[1] DNVGL-ST-N001. Marine operations and marine warranty. Technical Report, DNV GL; 2016.
[2] WAMIT INC. WAMIT user manual, version 6.4. Technical Report, WAMIT, INC.; 2009.
[3] Fathi DE. ShipX Vessel Responses (VERES), User's manual. Technical Report, SINTEF Ocean AS; 2018.
[4] Gourlay T, von Graefe A, Shigunov V, Lataire E. Comparison of AQWA, GL rankine, MOSES, OCTOPUS, PDStrip and WAMIT with model test results for cargo ship wave-induced motions in shallow water. In: Proceedings of the ASME 2015 34th International Conference on Ocean, Offshore and Arctic Engineering, Vol. 11. St. John's, Newfoundland, Canada; 2015.
[5] Tellkamp J, Bruns A, Gosch T, Günther H, Hansen PF, Nielsen UD, Papanikolaou A, Spanos D, Papatzanakis G, Kassner S, Wittkuhn D, Tränkmann I, Ehrke K-C, Krüger S, Vorhoelter H, Kluwe F, Jaap Struijk JKN. ADOPT summary of experiences and needs for further development. Technical Report, FORCE Technology and Uniresearch; 2009.
[6] Dannenberg J, Hessner K, Naaijen P, van den Boom H, Reichert K. The on board wave and motion estimator OWME. In: Proceedings of the 20th International Offshore and Polar Engineering Conference. International Society of Offshore and Polar Engineers; 2010.
[7] Clauss GF, Kosleck S, Testa D. Critical situations of vessel operations in short crested seas - forecast and decision support system. J Offshore Mech Arct Eng 2012;134(3). http://dx.doi.org/10.1115/1.4004515.
[8] Connell BSH, Rudzinsky JP, Brundick CS, Milewski WM, Kusters JG, Farquharson G. Development of an environmental and ship motion forecasting system. In: International Conference on Offshore Mechanics and Arctic Engineering, Volume 11: Prof. Robert F. Beck Honoring Symposium on Marine Hydrodynamics, 2015, http://dx.doi.org/10.1115/OMAE2015-42422.
[9] Naaijen P, van Oosten K, Roozen K, van't Veer R. Validation of a deterministic wave and ship motion prediction system. In: International Conference on Offshore Mechanics and Arctic Engineering, 2018, http://dx.doi.org/10.1115/OMAE2018-78037.
[10] ECMWF. Part VII: ECMWF wave model. In: IFS Documentation CY41R2. IFS Documentation, (7). ECMWF; 2016, URL: https://www.ecmwf.int/node/16651.
[11] Chan H-S, Armaoglu E, Thomson M, Garner A, Parisotto A, Sovilla S. Response forecasts for a suspended wellbay module and flare tower during transit to shore. In: The 29th International Ocean and Polar Engineering Conference. Honolulu, Hawaii, USA; 2019.
[12] Hilmer T, Thornhill E. Deterministic wave predictions from the wamos II. In: OCEANS 2014 - TAIPEI. 2014, p. 1–8.
[13] Stredulinsky DC, Thornhill EM. Ship motion and wave radar data fusion for shipboard wave measurement. J Ship Res 2011;55:73–85.
[14] Nouguier F, Grilli ST, Guérin C. Nonlinear ocean wave reconstruction algorithms based on simulated spatiotemporal data acquired by a flash LIDAR camera. IEEE Trans Geosci Remote Sens 2014;52(3):1761–71. http://dx.doi.org/10.1109/TGRS.2013.2254494.
[15] Nielsen UD. A concise account of techniques available for shipboard sea state estimation. Ocean Eng 2017;129:352–62. http://dx.doi.org/10.1016/j.oceaneng.2016.11.035.
[16] Ren Z, Han X, Verma AS, Dirdal JA, Skjetne R. Sea state estimation based on vessel motion responses: Improved smoothness and robustness using Bézier surface and L1 optimization. Mar Struct 2021;76:102904. http://dx.doi.org/10.1016/j.marstruc.2020.102904.
[17] Xu H, Soares CG. Hydrodynamic coefficient estimation for ship manoeuvring in shallow water using an optimal truncated LS-SVM. Ocean Eng 2019;191:106488.
[18] Fossen T, Sagatun S, Sørensen A. Identification of dynamically positioned ships. Control Eng Pract 1996;4(3):369–76. http://dx.doi.org/10.1016/0967-0661(96)00014-7.
[19] Kaasen KE, Berget K, Lie H, Bjørkli R. Automatic tuning of vessel models offshore: A feasibility study using high-precision data from model test. In: Offshore Technology Conference, (OTC-30690-MS). Houston, Texas, USA; 2020.
[20] Han X, Leira BJ, Sævik S. Vessel hydrodynamic model tuning by discrete Bayesian updating using simulated onboard sensor data. Ocean Eng 2021;220. http://dx.doi.org/10.1016/j.oceaneng.2020.108407, URL: https://www.sciencedirect.com/science/article/pii/S0029801820313147.
[21] Gelman A, Carlin J, Stern H, Dunson D, Vehtari A, Rubin D. Bayesian Data Analysis. third ed.. 2013.
[22] Han X, Leira BJ, Sævik S, Ren Z. Onboard tuning of vessel seakeeping model parameters and sea state characteristics. Mar Struct 2021;78. http://dx.doi.org/10.1016/j.marstruc.2021.102998.
[23] Julier SJ, Uhlmann JK. A general method for approximating nonlinear transformations of probability distributions. 1996.
[24] Julier SJ. The scaled unscented transformation. In: Proceedings of the 2002 American Control Conference (IEEE Cat. No. CH37301), Vol. 6. IEEE; 2002, p. 4555–9.
[25] ITTC. Recommended procedures and Guidelines: Global Loads Seakeeping Procedure. Technical Report, International Towing Tank Conference; 2011.
[26] Van Der Merwe R, et al. Sigma-point Kalman filters for probabilistic inference in dynamic state-space models (Ph.D. thesis), OGI School of Science & Engineering at OHSU; 2004.
[27] Han X, Sævik S, Leira BJ. A sensitivity study of vessel hydrodynamic model parameters. In: Proceedings of the ASME 2020 39th International Conference on Ocean, Offshore and Arctic Engineering, Vol. 1. Virtual, Online; 2020.
[28] Virtanen P, Gommers R, Oliphant TE, Haberland M, Reddy T, Cournapeau D, Burovski E, Peterson P, Weckesser W, Bright J, van der Walt SJ, Brett M, Wilson J, Millman KJ, Mayorov N, Nelson ARJ, Jones E, Kern R, Larson E, Carey CJ, Polat I, Feng Y, Moore EW, VanderPlas J, Laxalde D, Perktold J, Cimrman R, Henriksen I, Quintero EA, Harris CR, Archibald AM, Ribeiro AH, Pedregosa F, van Mulbregt P, and SciPy 10 Contributors. SciPy 1.0: Fundamental algorithms for scientific computing in python. Nature Methods 2020;17:261–72. http://dx.doi.org/10.1038/s41592-019-0686-2.
[29] Fathi DE. ShipX Vessel Responses (VERES), User's manual. echnical Report, SINTEF Ocean AS; 2018.
[30] Ommani B, Kristiansen T, Berget K. Investigating a simplified model for moonpool piston mode response in irregular waves. In: Proceedings of the ASME 2018 37th International Conference on Ocean, Offshore and Arctic Engineering. Madrid, Spain; 2018.
[31] Ravinthrakumar S, Kristiansen T, Ommani B. On the Hydrodynamic Interaction Between Ship and Free-Surface Motions on Vessels With Moonpools, In: Proceedings of the ASME 2019 38th International Conference on Ocean, Offshore and Arctic Engineering, Glasgow, Scotland, UK; 2019:.
[32] Ravinthrakumar S, Kristiansen T, Molin B, Ommani B. Coupled vessel and moonpool responses in regular and irregular waves. Appl Ocean Res 2020;96.
[33] Faltinsen OM. Sea Loads on Ships and Offshore Structures. New York: Cambridge University Press Cambridge; 1990.
[34] ITTC. Recommended procedures and Guidelines: Numerical Estimation of Roll Damping. Technical Report, International Towing Tank Conference; 2011.
[35] Kaplan P. Lecture notes on nonlinear theory of ship roll motion in a random seaway. 1966.
[36] Han X, Sævik S, Leira BJ. Tuning of vessel parameters including sea state dependent roll damping. Ocean Eng 2021;233. http://dx.doi.org/10.1016/j.oceaneng.2021.109084.
[37] Fathi DE, Hoff JR. ShipX Vessel Responses (VERES), Theory manual. Technical Report, SINTEF Ocean AS; 2017.
[38] Ikeda Y. On roll damping force of ship - effect of friction of hull and normal force of bilge keels. Technical Report 00401, Osaka Prefecture University; 1978.
[39] Ikeda Y, Himeno Y, Tanaka N. On eddy making component of roll damping force on naked hull. Technical Report 00403, Osaka Prefecture University; 1978.
[40] Ikeda Y, Komatsu K, Tanaka N. On roll damping force of ship-effects of hull surface pressure created by bilge keels. Technical Report 00402, Osaka Prefecture University; 1979.
[41] Rezende FC, Chen XB, Ferreira MD. Second order roll motions for fpso's operating in severe environmental conditions. In: Offshore Technology Conference, Number OTC-18906-MS, Houston, Texas, USA; 2007, http://dx.doi.org/10.4043/18906-MS.
[42] Dhavalikar SS. Comparative study of seakeeping analysis results from various methods. In: Proceedings of the ASME 2011 30th International Conference on Ocean, Offshore and Arctic Engineering. Volume 1: Offshore Technology; Polar and Arctic Sciences and Technology, 2011, p. 217–23. http://dx.doi.org/10.1115/OMAE2011-49223.